Composites Part B 328 (2027) 114145

Contents lists available at ScienceDirect

Composites Part B

journal homepage: www.elsevier.com/locate/composites

An enhanced kinematic forming framework for fast and accurate prediction of in-plane strains in unidirectional fabrics

Peter Hede Broberg [a,*], Christian Krogh [b], Bastian Schäfer [c], Jan Paul Wank [d], Luise Kärger [d], Brian Lau Verndal Bak [a], Esben Lindgaard [a]

[a] CraCS Research Group (cracs.aau.dk), Department of Materials and Production, Aalborg University, Fibigerstræde 16, DK-9220, Aalborg East, Denmark
[b] Siemens Gamesa Renewable Energy, Assensvej 11, 9220 Aalborg East, Denmark
[c] Simutence GmbH, 76131 Karlsruhe, Germany
[d] Karlsruhe Institute of Technology (KIT), FAST - Lightweight Engineering, 76131 Karlsruhe, Germany

ARTICLE INFO

Dataset link: KinDrape3D (Original data)

Keywords:
Forming process
UD fabrics
Kinematic modelling
Composite manufacturing

ABSTRACT

Unidirectional (UD) fabrics are attractive for high-performance structures due to their high stiffness-to-weight ratio. However, realising these benefits in components with curved geometries requires accurate prediction of forming behaviour to control manufacturing-induced defects and obtain reliable fibre orientations for structural analysis. Existing finite element forming models capture relevant deformation mechanisms but are computationally expensive, limiting applicability in large-scale optimisation and parametric design studies increasingly required in industrial development cycles. Kinematic forming models offer a computationally efficient alternative, but existing approaches are largely limited to pure-shear assumptions that are unsuitable for UD fabrics, while simple-shear formulations have received limited attention and algorithmic development and generally cannot represent transverse deformation. To address these limitations, this paper presents a kinematic forming framework based on simple-shear kinematics with an experimentally calibrated shear-dependent fibre spacing. The framework employs robust geometric intersection algorithms to construct fibre paths on single-valued surfaces and introduces a new enhanced simple-shear model capable of representing both shear and deformation perpendicular to fibres in UD non-crimp fabrics (UD-NCFs). The simple-shear formulation is verified against analytical hemispherical forming solutions, while the enhanced simple-shear model is calibrated using a 0° UD-NCF forming case and validated against a 45° UD-NCF forming case through comparison with experiments and high-fidelity finite element simulations. The proposed framework accurately predicts deformed geometry and geometrically-derived in-plane strain fields while achieving speed-up factors of 134-251 compared with finite element simulations. The kinematic framework is therefore well suited for optimisation and early-stage design studies. The software implementation is freely available at https://doi.org/10.5281/zenodo.22044780.

1. Introduction

Composite materials are widely used in high-performance lightweight structures across aerospace, marine, automotive, and wind-energy applications due their high specific stiffness and strength. Their excellent mechanical properties, however, come with complex manufacturing routes that typically involve several sequential processing steps. Among these, liquid composite moulding (LCM) has become increasingly attractive due to its cost efficiency and substantially lower energy consumption compared to autoclave-based processing [1–3]. In LCM, dry textile reinforcements are first formed over the mould, then impregnated with a liquid resin, followed by curing and demoulding. The forming step plays a decisive role in the final structural performance, as it governs the resulting fibre orientation and may introduce defects such as wrinkles or fibre waviness that can degrade mechanical properties [4–9].

Within the broad class of reinforcements, non-crimp fabrics (NCFs) provide significant lightweight potential relative to their woven counterpart because of their low crimp and high alignment [10,11]. The same features, however, may reduce their formability and increase their susceptibility to defects during draping [12–14]. The forming of unidirectional (UD) NCFs is especially complex, as the macroscopic forming response and defect formation is strongly influenced by the fabric

* Corresponding author.
E-mail addresses: phb@mp.aau.dk (P.H. Broberg), christian.ck.krogh@siemensgamesa.com (C. Krogh), bastian.schaefer@simutence.de (B. Schäfer), jan.wank@kit.edu (J.P. Wank), luise.kaerger@kit.edu (L. Kärger), brianbak@mp.aau.dk (B.L.V. Bak), elo@mp.aau.dk (E. Lindgaard).

https://doi.org/10.1016/j.compositesb.2026.114145
Received 3 July 2026; Received in revised form 21 August 2026; Accepted 23 August 2026
Available online 31 August 2026

architecture leading to specific deformation modes such as fibre/yarn sliding, yarn friction, yarn compression and gapping, and stitch deformation [13,15]. Accurately predicting the resulting fibre orientations and the onset of manufacturing-induced defects is therefore essential to ensure robust design and process development.

Computational forming models offer an efficient alternative to trial-and-error experimentation, shortening development time and cost. Fast and reliable forming predictions are vital as industrial design cycles increasingly incorporate optimisation and virtual process chains [16]. Existing modelling approaches can be grouped into three categories: mechanical models, machine-learning-based (data-driven) models, and kinematic (mapping) models.

Mechanical models are typically implemented in finite-element frameworks at either the macroscale [8,17–20] or micro- and mesoscale [21–23]. For UD-NCF forming, macroscale finite-element models are attractive because they can incorporate material-specific constitutive behaviour, process conditions, and represent critical deformation modes such as in-plane and out-of-plane shearing, and wrinkle formation [19,20]. However, their computational cost limits their use in optimisation loops, large structure analysis, such as wind turbine blades, and iterative design studies. In addition, accurately representing yarn sliding, asymmetric shear response, and local yarn rearrangement in UD-NCFs remains challenging in conventional continuum formulations.

Machine-learning models [24–29] have emerged as alternatives to reduce computational cost by acting as fast surrogates for experiments or high-fidelity simulations. However, these models depend strongly on training data and generally lack robustness outside the training domain. Recent machine learning approaches based on graph neural networks have shown promising potential for scalability to general geometries and material systems [30], but still rely on large training datasets to achieve accurate predictions. This data dependence, combined with limited physical interpretability, currently restricts their applicability in early-stage design of UD-NCF forming processes where extensive training data may not be available.

Kinematic models, also referred to as mapping or geometric approaches, provide an effective alternative by imposing simplified, physically motivated deformation constraints to generate rapid forming predictions [31–33]. They require neither detailed constitutive laws nor training data and are therefore well suited for early-stage design, parameter studies, and optimisation. Conventional kinematic models assume inextensible fibres along warp and weft directions with free rotation at cross-over points, leading to pure-shear (trellis) deformation [34]. This assumption captures the behaviour of woven fabrics and biaxial NCFs well, but it cannot represent the fibre sliding and deformation mechanisms observed during deformation of unidirectional fabric [35–38]. To model UD-NCF forming within a kinematic framework, simple-shear kinematics are therefore required, together with an additional description of transverse fibre spacing.

Although algorithms for pure-shear mapping are well documented [32,33,39–42], kinematic draping based on simple-shear has largely been presented at a conceptual level [32,43–45]. To the authors' knowledge, the corresponding numerical realisations are mostly described in an abstract sense, providing limited detail for reproduction and generalisation. Commercial draping solvers, such as ANSYS ACP, permit UD fabric draping, however their implementation relies on energy minimisation procedures [46] that are not directly derived from kinematic admissibility conditions, thereby introducing deformation modes through numerical regularisation rather than explicit physical constraints. Moreover, the classical simple-shear description cannot represent the transverse strain behaviour observed experimentally in UD-NCFs during forming [13], which further limits the applicability of existing kinematic models to UD reinforcements.

This work addresses these gaps by developing a kinematic forming framework for unidirectional fabrics on mould geometries described by single-valued surfaces. The objective is to enable fast prediction of deformed geometry and in-plane strain measures for UD fabrics, while retaining the key deformation mechanisms observed during forming. The novelty of the work consists of two distinct contributions. First, a new fibre-tracking algorithm is introduced for applying simple-shear kinematics to double curved mould surfaces. The algorithm constructs fibre paths through intersections between geometric primitives and the mould surface, providing an explicit and reproducible procedure for simple-shear draping simulations. Second, an enhanced simple-shear model is proposed to account for transverse fibre-spacing changes observed experimentally in UD-NCF forming [13]. This is achieved through a experimentally-calibrated phenomenological shear–spacing relation that links the local fibre shear angle to the spacing between neighbouring fibres. The framework is verified against analytical solutions for classical simple-shear, while the enhanced formulation is calibrated using a UD-NCF [0°] forming case and validated against a UD-NCF [45°] forming case, through comparisons with experimental measurements and high-fidelity FE simulations. A software implementation of the proposed framework is freely available at https://doi.org/10.5281/zenodo.22044780.

The remainder of this paper is organised as follows. Section 2 presents the kinematic framework, including the fibre-tracking algorithm, strain measures, shear–spacing relations, and validation setup. Section 3 verifies the simple-shear and enhanced simple-shear formulations, calibrates the shear–spacing relation, and compares the resulting predictions with experimental data and high-fidelity FE simulations. Section 4 discusses the modelling implications, limitations, and applicability of the framework, and Section 5 summarises the main conclusions.

2. Methods

An overview of the proposed kinematic forming framework is shown in Fig. 1. The framework builds on the open-source kinematic draping tool *KinDrape* [33] and employs the same algorithm for constructing generator cells. The present work extends this approach beyond pure-shear kinematics by introducing simple-shear and enhanced simple-shear kinematic models. The framework is implemented in an open-source Python code, which is freely available at https://doi.org/10.5281/zenodo.22044780.

The inputs to the single-layer kinematic forming analysis consist of the mould geometry, a set of fabric parameters, and initial conditions. The mould geometry is defined as a single-valued surface function $F(x, y) = z$, excluding vertical walls, undercuts, and multiply valued geometries. The geometry may be specified analytically or obtained from an interpolated point cloud. The fabric is characterised by its width (W), length (L), discretisation distance (d), fabric orientation (θ), and the kinematic behaviour of the fabric (either pure-shear, simple-shear, or enhanced simple-shear). The initial conditions are defined by the origin point on the mould (x_0, y_0), the corresponding origin point on the fabric given in local fabric coordinates (s, u), and initial fibre direction. Optional numerical stabilisation strategies and model parameters can also be specified and are detailed in Sections 2.4 and 2.5. The output of the kinematic forming analysis is the deformed fabric configuration mapped onto the mould surface. Based on this configuration, three in-plane strain measures are evaluated. These are purely geometrically derived and are defined in the following subsection.

2.1. In-plane strain measures

The kinematic forming analysis provides the deformed fabric configuration on the mould surface, from which three in-plane strain measures are derived: the shear angle (γ), the transverse strain (E_{22}), and the perpendicular strain ($E_{\perp}$). Please note that E_{22} and $E_{\perp}$ are geometrically evaluated as cell-based strain measures and are used to quantify changes in transverse and perpendicular fibre spacing, respectively, to enable comparison with the experimental results in [13]. All

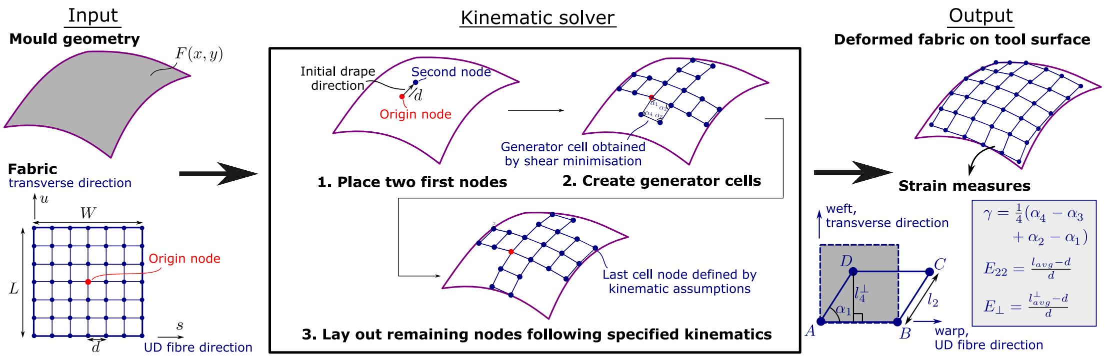

Fig. 1. Overview of the kinematic framework. The input to the framework is the mould geometry given as a function $z = F(x, y)$ and a fabric described by parameters length L, width W, discretisation d, start point, and kinematic assumptions. This is passed on to the kinematic solver, which maps the fabric to the mould surface.
Source: The figure of the kinematic solver is based on [33].

measures are evaluated on each quadrilateral cell as illustrated in Fig. 1.

The shear angle (γ) is defined based on the deviation of the internal cell angles from a right angle and is computed as,

$$\gamma = \frac{1}{4}\sum_{i=1}^{4}(\alpha_i - 90^\circ)\cdot(-1)^i, \tag{1}$$

where α_i are the internal angles at the four vertices of the cell defined by $\alpha_1 = \angle DAB$, $\alpha_2 = \angle ABC$, $\alpha_3 = \angle BCD$, and $\alpha_4 = \angle CDA$. The alternating sign ensures that both positive and negative shear can be represented consistently. The sign convention used throughout this work is illustrated in Fig. 1, where the depicted shear is positive.

The transverse strain (E_{22}) is defined as the relative change in the average distance between neighbouring fibres in the transverse direction:

$$E_{22} = \frac{l_{\text{avg}} - d}{d}, \quad l_{\text{avg}} = \frac{1}{2}(\|\vec{AD}\| + \|\vec{BC}\|), \tag{2}$$

where d is the initial fibre spacing/discretisation, l_{avg} is the average transverse distance between neighbouring fibres in the deformed configuration, and $\vec{AD}$ and $\vec{BC}$ (denoted l_2 in Fig. 1) are the transverse edges of the deformed cell. Note that the fibre orientation changes during deformation, which results in the transverse strain not describing fibre spacing. Fibre spacing is instead accounted for with the perpendicular strain ($E_{\perp}$) [13].

The perpendicular strain ($E_{\perp}$) is defined as the change in spacing normal to the fibre direction and is computed from the average of four point-to-fibre distances within the cell:

$$E_{\perp} = \frac{l^{\perp}_{\text{avg}} - d}{d}, \quad l^{\perp}_{\text{avg}} = \frac{1}{4}(l^{\perp}_1 + l^{\perp}_2 + l^{\perp}_3 + l^{\perp}_4). \tag{3}$$

Here, $l^{\perp}_i$ denotes the shortest distance from a cell vertex to the opposite fibre segment. For example, $l^{\perp}_4 = \frac{\|\vec{AD}\times\vec{AB}\|}{\|\vec{AB}\|}$, which corresponds to the height of a parallelogram defined by the vectors $\vec{AD}$ and $\vec{AB}$. This geometric interpretation is illustrated in Fig. 1.

2.2. Kinematic solver workflow and kinematic assumptions

The kinematic forming framework follows a three-step workflow, which is illustrated in Fig. 1 and summarised below:

1. The initial two nodes are placed on the mould surface based on the prescribed origin point on the mould, corresponding origin node on the fabric, initial draping direction, and distance d.
2. Generator cells defining the initial fibre paths are constructed. Starting from the origin, these cells are generated sequentially by minimising the local cell shear angle, which is equivalent to minimising the tangential curvature and thus enforcing a geodesic path on the mould surface.

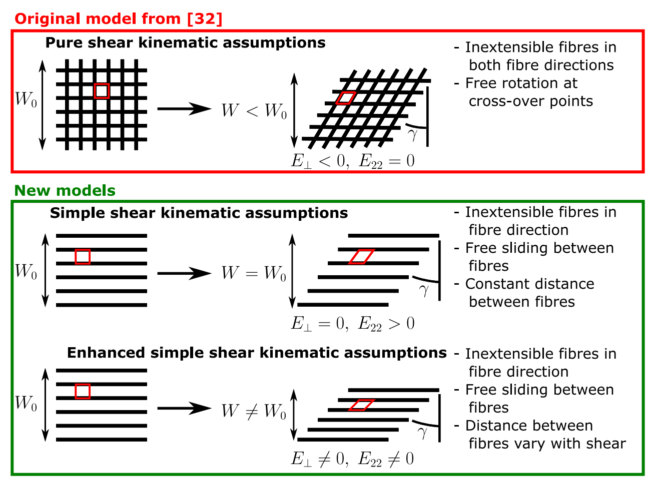

Fig. 2. Kinematic assumptions underlying the fabric models considered in this work. The pure-shear model is from [33] and the simple-shear and enhanced simple-shear models are new in this work.

3. The remaining cells are placed subject to the selected kinematic model and constrained by the generator cells. The different kinematic models are described below and are pure-shear, simple-shear, and enhanced simple-shear.

The present work focuses on the development of new kinematic models associated with Step 3. Details of Steps 1 and 2 are available in [33] and are therefore not repeated here.

Three kinematic models are implemented in the proposed framework, which are illustrated in Fig. 2:

- **Pure-shear model:** The conventional kinematic draping model assumes that yarns are free to rotate at cross-over points, that no slip occurs at these points, and that yarns in both warp and weft directions are inextensible. Consequently, transverse strain is zero, while a negative perpendicular strain develops under shear. This model accurately represents the forming behaviour of woven fabrics and biaxial non-crimp fabrics (BIAX-NCFs), and may also be applied to quasi-unidirectional NCFs at low shear angles [36].
- **Simple-shear model:** This model assumes that the fabric consists of unidirectional fibres that are free to slide relative to each other during deformation while maintaining a constant fibre spacing. As a result, the perpendicular strain is zero, the transverse strain is positive, and the in-plane shear angle directly reflects the relative sliding between fibres. While suitable for idealised simple-shear

deformation of UD fabrics, this formulation cannot represent the perpendicular strains observed experimentally in UD-NCFs [13] and may require appropriate stabilisation to satisfy the constant spacing constraint. A robust geometric implementation of this model is developed in the present work.

- **Enhanced simple-shear model:** Extending the simple-shear formulation, this model replaces the constant fibre spacing constraint with a function that maps shear deformation to fibre distance. This enables the representation of combined shear and perpendicular strain deformation modes observed in UD-NCFs during forming [13]. The transverse deformation is governed by a shear–spacing relation introduced in Section 2.5. This approach constitutes a novel kinematic model and enables fast yet accurate simulation of UD-NCF forming processes.

In the following subsections, the detailed numerical algorithms associated with the different kinematic models are described in detail. All solvers operate on the geodesic generator cells from Step 2 of the workflow.

The placement of new points $\boldsymbol{p}_{i,j}$ in Step 3 is formulated as a geometric intersection problem, where i and j denote discrete indices in the fibre and transverse directions, respectively; for simple shear modelling, i identifies the fibre number, while j denotes the material point along the fibre. Candidate points are defined along an intersection curve that satisfies the prescribed kinematic constraints, expressed in a local coordinate system (l) and mapped to global coordinates (g) by,

$$\boldsymbol{p}^{(\mathrm{g})} = \begin{bmatrix} p_{\mathrm{x}}^{(\mathrm{g})} \\ p_{\mathrm{y}}^{(\mathrm{g})} \\ p_{\mathrm{z}}^{(\mathrm{g})} \end{bmatrix} = \boldsymbol{o}_{\mathrm{l}} + \boldsymbol{R}_{\mathrm{l}}\boldsymbol{p}^{(\mathrm{l})}, \quad \boldsymbol{R}_{\mathrm{l}} = [\hat{\boldsymbol{u}}_{\mathrm{l}},\ \hat{\boldsymbol{v}}_{\mathrm{l}},\ \hat{\boldsymbol{w}}_{\mathrm{l}}], \tag{4}$$

where $\boldsymbol{o}_{\mathrm{l}}$ denotes the origin of the local coordinate system and $\hat{\boldsymbol{u}}_{\mathrm{l}}$, $\hat{\boldsymbol{v}}_{\mathrm{l}}$, $\hat{\boldsymbol{w}}_{\mathrm{l}}$ are its orthonormal basis vectors.

A scalar residual function is introduced to enforce contact with the mould surface:

$$r(t) = p_{\mathrm{z}}^{(\mathrm{g})}(t) - F\left(p_{\mathrm{x}}^{(\mathrm{g})}(t),\ p_{\mathrm{y}}^{(\mathrm{g})}(t)\right), \tag{5}$$

where t parametrises the function. The candidate points which contact the mould surface and lie on the intersection curve correspond to the roots of $r(t) = 0$, which are computed using a bisection method [47].

2.3. Pure-shear algorithm

The pure-shear algorithm corresponds to the conventional kinematic draping formulation and is described in [33,40]. It is briefly summarised here for completeness. Given three known points within a quadrilateral cell, the remaining point is computed by enforcing inextensibility along both yarn directions. This is achieved by locating the unknown point at the intersection of two spheres of radius d, as illustrated in Fig. 3.

The intersection of the two spheres defines a circle with the centre $\boldsymbol{c}^{(\mathrm{g})}$ and radius r defined by,

$$\boldsymbol{c}^{(\mathrm{g})} = \frac{\boldsymbol{p}_{i-1,j}^{(\mathrm{g})} + \boldsymbol{p}_{i,j-1}^{(\mathrm{g})}}{2}, \quad r = \sqrt{d^2 - |\boldsymbol{c}^{(\mathrm{g})} - \boldsymbol{p}_{i-1,j}^{(\mathrm{g})}|^2}. \tag{6}$$

The local orthonormal coordinate system is introduced with origin at $\boldsymbol{c}^{(\mathrm{g})}$ and the basis vectors defined by,

$$\hat{\boldsymbol{u}}_{\mathrm{l}} = \frac{\boldsymbol{p}_{i-1,j-1}^{(\mathrm{g})} - \boldsymbol{c}^{(\mathrm{g})}}{|\boldsymbol{p}_{i-1,j-1}^{(\mathrm{g})} - \boldsymbol{c}^{(\mathrm{g})}|}, \quad \hat{\boldsymbol{w}}_{\mathrm{l}} = \frac{\boldsymbol{p}_{i-1,j}^{(\mathrm{g})} - \boldsymbol{c}^{(\mathrm{g})}}{|\boldsymbol{p}_{i-1,j}^{(\mathrm{g})} - \boldsymbol{c}^{(\mathrm{g})}|}, \tag{7}$$

$$\hat{\boldsymbol{v}}_{\mathrm{l}} = \frac{\hat{\boldsymbol{w}}_{\mathrm{l}} \times \hat{\boldsymbol{u}}_{\mathrm{l}}}{|\hat{\boldsymbol{w}}_{\mathrm{l}} \times \hat{\boldsymbol{u}}_{\mathrm{l}}|}.$$

The intersection circle is then parameterised in local coordinates as,

$$\boldsymbol{p}^{(\mathrm{l})}(t) = \begin{bmatrix} r\cos(t) \\ r\sin(t) \\ 0 \end{bmatrix}, \tag{8}$$

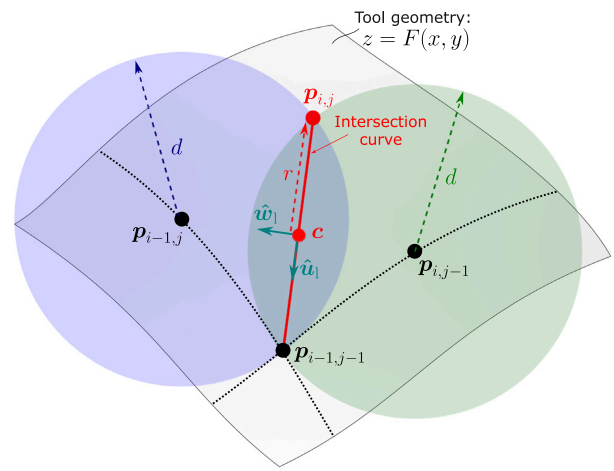

Fig. 3. Computation of a new point ($\boldsymbol{p}_{i,j}$) from three known neighbouring points under pure-shear assumptions. The new point lies on the intersection curve of two spheres of radius d. The dotted lines represent fibre paths. The intersection curve is a circle in three dimensions, which appears as a line in this two-dimensional projection.

where t is the scalar parameter of the candidate curve defined in Eq. (5). The parameter is restricted to the interval $\pi/3 < t < 5\pi/3$ to ensure selection of the physically admissible solution. This restriction excludes the mirror solution corresponding to the alternative intersection point located at $\boldsymbol{p}_{i-1,j-1}^{(\mathrm{g})}$. The admissible value of t is subsequently identified by enforcing intersection with the mould surface.

2.4. Simple-shear algorithm

In contrast to the pure-shear formulation, the simple-shear model does not represent the fabric as a pin-jointed net. Instead, it treats the fabric as a set of unidirectional fibres that are free to slide relative to one another during deformation. The defining kinematic constraint in the simple-shear algorithm is that the perpendicular spacing between neighbouring fibres remains constant, while fibre lengths are not explicitly enforced during the mapping process. The simple-shear algorithm therefore proceeds in two steps to satisfy both constant fibre spacing and inextensible fibres. First, individual fibres are mapped onto the mould surface subject to the constant spacing constraint, without enforcing fibre length. Once the fibres have been constructed, the quadrilateral cells and associated strain measures are recovered from the resulting fibre network using the discretisation distance d as illustrated in Fig. 4. This separation enables a robust geometric formulation of simple-shear kinematics.

A new point $\boldsymbol{p}_{i,j}^{(\mathrm{g})}$ along fibre i is computed using three known points on the neighbouring fibre $(i-1)$ by enforcing a constant fibre spacing. Geometrically, this is achieved by locating the unknown point at the intersection of two cylinders of radius r_{cyl}, as illustrated in Fig. 5. For the simple-shear model, the cylinder radius corresponds to the initial fibre spacing ($r_{\mathrm{cyl}} = d$), while this radius may vary for the enhanced simple-shear model introduced in Section 2.5. Each cylinder is centred on a known fibre segment, such that the perpendicular distance between fibres is preserved.

The cylinder axes are defined as,

$$\boldsymbol{z}_1 = \boldsymbol{p}_{i-1,j}^{(\mathrm{g})} - \boldsymbol{p}_{i-1,j-1}^{(\mathrm{g})}, \tag{9}$$

$$\boldsymbol{z}_2 = \boldsymbol{p}_{i-1,j+1}^{(\mathrm{g})} - \boldsymbol{p}_{i-1,j}^{(\mathrm{g})}, \tag{10}$$

and the angle θ between the two axes is given by,

$$\theta = \cos^{-1}\left(\frac{\boldsymbol{z}_1 \cdot \boldsymbol{z}_2}{|\boldsymbol{z}_1|\ |\boldsymbol{z}_2|}\right). \tag{11}$$

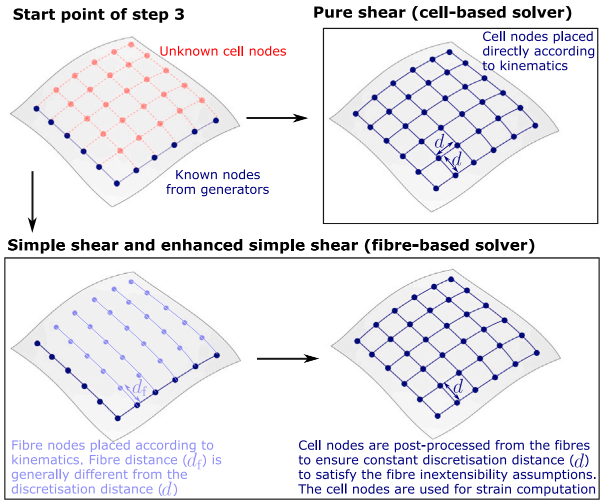

Fig. 4. The simple-shear and enhanced simple-shear algorithm consists of two steps. The first step is the laying out of the fibres satisfying the fibre distance constraint, while the second step post-process cell nodes on the fibres to satisfy fibre in-extensibility.

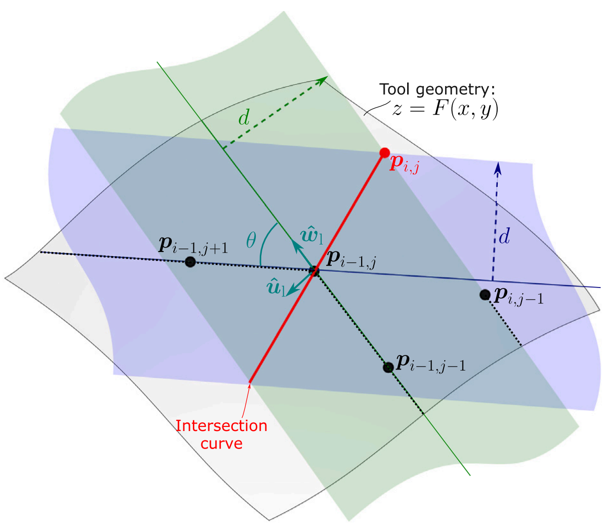

Fig. 5. Computation of a new point ($\boldsymbol{p}^{(g)}_{i,j}$) along under simple-shear assumptions. The new point is located on the intersection curve of two cylinders defined by three neighbouring points on an adjacent fibre. The dotted lines represent fibre paths. The intersection curve is a circle in three dimensions, which appears as a line in this two-dimensional projection.

A local orthonormal coordinate system is introduced with origin at $p^{(g)}_{i-1,j}$ and basis vectors,

$$\hat{\boldsymbol{w}}_1 = \frac{\boldsymbol{z}_1}{|\boldsymbol{z}_1|}, \quad \hat{\boldsymbol{v}}_1 = \frac{\boldsymbol{z}_1 \times \boldsymbol{z}_2}{|\boldsymbol{z}_1 \times \boldsymbol{z}_2|}, \quad \hat{\boldsymbol{u}}_1 = \frac{\hat{\boldsymbol{v}}_1 \times \hat{\boldsymbol{w}}_1}{|\hat{\boldsymbol{v}}_1 \times \hat{\boldsymbol{w}}_1|}. \tag{12}$$

The intersection curve between the two cylinders can be parameterised in local coordinates as

$$\boldsymbol{p}^{(l)}(t) = \begin{bmatrix} r_{\text{cyl}} \cos(t) \\ r_{\text{cyl}} \sin(t) \\ r_{\text{cyl}} \cos(t)(\cot(\theta) + \csc(\theta)) \end{bmatrix}, \tag{13}$$

with $0 < t < 2\pi$. The derivation of this expression is provided in Appendix A. For a general mould geometry, the intersection curve may yield two candidate points that both satisfy the constant-spacing constraint and intersect the mould surface. One candidate lies on the fibre preceding the neighbouring fibre used to define the cylinders, and is therefore a geometrically valid but non-physical solution, as it results in the fabric collapsing. The other candidate is the physical admissible solution, which satisfies kinematic constraints and advances the new fibre, as illustrated in Fig. 5.

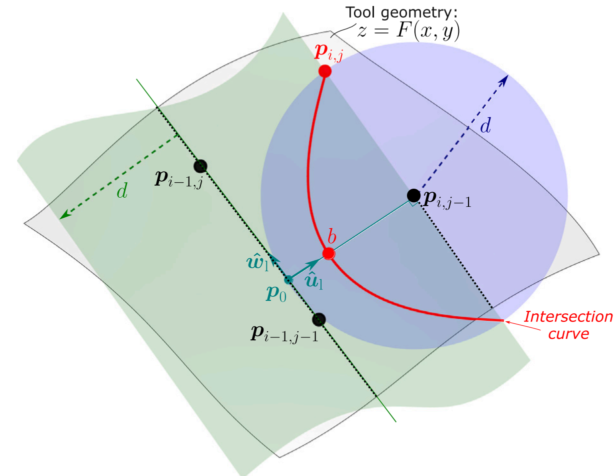

Fig. 6. Cylinder–sphere intersection used to compute the final point in a fibre ($\boldsymbol{p}^{(g)}_{i,j}$) when insufficient neighbouring points are available for a cylinder–cylinder intersection. The dotted lines represent fibre paths.

The cylinder–cylinder intersection requires three neighbouring points in the previous fibre and may become ill-conditioned when the angle θ between the cylinder axes is small. In addition, only two neighbouring points are available when computing the final point along a fibre. In these cases, a cylinder–sphere intersection is employed, as illustrated in Fig. 6.

The cylinder axis is defined as

$$\boldsymbol{z}_1 = \boldsymbol{p}^{(g)}_{i-1,j} - \boldsymbol{p}^{(g)}_{i-1,j-1}, \tag{14}$$

and a local coordinate system is introduced with origin $\boldsymbol{p}^{(g)}_0$ given by

$$\boldsymbol{p}^{(g)}_0 = \boldsymbol{p}^{(g)}_{i-1,j-1} + \hat{\boldsymbol{w}}_1 t_0, \tag{15}$$
$$t_0 = (\boldsymbol{p}^{(g)}_{i,j-1} - \boldsymbol{p}^{(g)}_{i-1,j-1}) \cdot \hat{\boldsymbol{w}}_1.$$

The orthonormal basis vectors are defined as,

$$\hat{\boldsymbol{w}}_1 = \frac{\boldsymbol{z}_1}{|\boldsymbol{z}_1|}, \quad \hat{\boldsymbol{u}}_1 = \frac{\boldsymbol{p}_{i,j-1} - \boldsymbol{p}_0}{|\boldsymbol{p}_{i,j-1} - \boldsymbol{p}_0|}, \quad \hat{\boldsymbol{v}}_1 = \frac{\hat{\boldsymbol{w}}_1 \times \hat{\boldsymbol{u}}_1}{|\hat{\boldsymbol{w}}_1 \times \hat{\boldsymbol{u}}_1|}. \tag{16}$$

The intersection curve between the cylinder and sphere is parameterised as

$$\boldsymbol{p}^{(l)}(t) = \begin{bmatrix} r_{\text{cyl}} \cos(t) \\ r_{\text{cyl}} \sin(t) \\ \sqrt{2a(x-b)} \end{bmatrix}, \tag{17}$$

where

$$a = |\boldsymbol{p}^{(g)}_0 - \boldsymbol{p}^{(g)}_{i-1,j-1}|, \quad b = \frac{a^2 + r^2_{\text{cyl}} - d^2}{2a}. \tag{18}$$

The derivation of this intersection is provided in Appendix A.

The fibre-tracking algorithm is summarised in Algorithm 1. The cylinder–cylinder conditions are considered satisfied when three neighbouring points are available on the previously constructed fibre and the angle between the cylinder axes satisfies $\theta > \theta_{\min}$, with $\theta_{\min} = 5°$ in the present work. The bisection search is terminated when the residual function of Eq. (5) is less than 5×10^{-6} in the length units of the geometry. If no roots are found, the kinematic assumptions are not satisfied and the software gives a warning. The subsequent placement of cell nodes along the tracked fibres is summarised in Algorithm 2. Auxiliary points are only introduced when the tracked fibre has become shorter than the required nodal distance due to curvature-based point removal, which is described in the following section.

Algorithm 1 Fibre tracking for simple-shear and enhanced simple-shear models

Input: Generator cells, mould surface $z = F(x, y)$, initial fibre spacing d_0, target fibre length L_0
Output: Set of tracked fibres
Initialise the first fibre from the generator cells
for each new fibre i **do**
  Initialise fibre i from corresponding generator point
  Set accumulated fibre length $L_{\text{fiber}} = 0$
  while $L_{\text{fiber}} < L_0$ **do**
    if enhanced simple-shear model is used **then**
      Compute the local fibre shear angle ϕ
      Compute the target spacing $d_{\text{new}} = d(\phi)$
      Apply damping to obtain the spacing d
    else
      Set spacing $d = d_0$ (simple-shear)
    end if
    if cylinder-cylinder conditions are true **then**
      Construct the cylinder-cylinder intersection
    else
      Construct the cylinder-sphere intersection
    end if
    Locate intersection-surface roots by bisection
    Select admissible branch from fibre ordering
    Append the accepted point to fibre i
    Update L_{fiber} from the newest fibre segment
  end while
  Store fibre i
end for

Algorithm 2 Node placement along tracked fibres

Input: Tracked fibre points $\{p_k\}$, target node distance L_{node}
Output: Node position p_{node}
if $L_{\text{node}} = 0$ **then**
  Return the first fibre point
end if
Set accumulated length $L_{\text{acc}} = 0$
for each consecutive fibre segment (p_k, p_{k+1}) **do**
  Compute the segment length

$$L_{\text{seg}} = \|p_{k+1} - p_k\|$$

  if $L_{\text{acc}} + L_{\text{seg}} \geq L_{\text{node}}$ **then**
    Compute the interpolation ratio

$$\lambda = \frac{L_{\text{node}} - L_{\text{acc}}}{L_{\text{seg}}}$$

    Interpolate the node position

$$p_{\text{node}} = (1 - \lambda)p_k + \lambda p_{k+1}$$

    Return p_{node}
  end if
  Update $L_{\text{acc}} = L_{\text{acc}} + L_{\text{seg}}$
end for
Extrapolate auxiliary point from final segment
Return the auxiliary point

2.4.1. *Simple-shear stabilisations*

Although the kinematic assumptions underlying simple-shear are conceptually straightforward, their numerical implementation can be unstable for general mould geometries. These instabilities arise because fibre length is not explicitly constrained during fibre tracking with the cylinder–cylinder intersection, which may lead to overly large or excessively small steps between successive fibre points. To ensure numerical robustness and stable fibre construction, three stabilisation strategies are employed. These are illustrated in Fig. 7.

Removal of spurious points. The first stabilisation eliminates spurious points that arise from overly large advancement steps during fibre tracking, which may cause a point to deviate from the local fibre path, as shown in Fig. 7(a). For each newly proposed point $\boldsymbol{p}_{i,j+1}^{(g)}$, two vectors are defined,

$$\boldsymbol{v}_1 = \boldsymbol{p}_{i,j}^{(g)} - \boldsymbol{p}_{i,j-1}^{(g)}, \tag{19}$$

$$\boldsymbol{v}_2 = \boldsymbol{p}_{i,j+1}^{(g)} - \boldsymbol{p}_{i,j}^{(g)}. \tag{20}$$

If the dot product $\boldsymbol{v}_1 \cdot \boldsymbol{v}_2$ is negative, the angle between the vectors are obtuse and the intermediate point $\boldsymbol{p}_{i,j}^{(g)}$ is identified as spurious and removed. This criterion ensures monotonic progression along the fibre and prevents local reversals in fibre direction.

Fibre segment length averaging. The second stabilisation limits overshooting during fibre construction by locally averaging the fibre segment length, as illustrated in Fig. 7(b). When the cylinder-sphere intersection is used, the sphere radius is adjusted according to neighbouring fibre segments to avoid $\boldsymbol{p}_{i,j}$ becoming spurious by laying ahead of $\boldsymbol{p}_{i,j+1}$,

$$r = (\delta_j + \delta_{j+1})/2, \tag{21}$$

where

$$\delta_j = |\boldsymbol{p}_{i-1,j+1}^{(g)} - \boldsymbol{p}_{i-1,j}^{(g)}|, \tag{22}$$

$$\delta_{j+1} = |\boldsymbol{p}_{i-1,j+2}^{(g)} - \boldsymbol{p}_{i-1,j+1}^{(g)}|. \tag{23}$$

This averaging smooths variations in step length between neighbouring fibres and improves numerical stability without altering the prescribed kinematic constraints.

Curvature-based point removal. The final stabilisation is applied after an entire fibre has been constructed and before advancing to the next fibre. This stabilisation is thus performed after the other stabilisations. It removes points associated with excessive local curvature, which typically result from small discretisation distances and large mould curvatures. For each interior point, $\boldsymbol{p}_{i,j}^{(g)}$, the curvature is estimated from the radius R of the circumcircle passing through the three consecutive points $\boldsymbol{p}_{i,j-1}^{(g)}$, $\boldsymbol{p}_{i,j}^{(g)}$, and $\boldsymbol{p}_{i,j+1}^{(g)}$,

$$\kappa_i = \frac{1}{R_i} = \frac{4A_i}{a_i b_i c_i}, \tag{24}$$

where the triangle area A_i is obtained from,

$$\|\boldsymbol{v}_1 \times \boldsymbol{v}_2\| = 2A_i, \tag{25}$$

with

$$\boldsymbol{v}_1 = \boldsymbol{p}_{i,j}^{(g)} - \boldsymbol{p}_{i,j-1}^{(g)}, \tag{26}$$

$$\boldsymbol{v}_2 = \boldsymbol{p}_{i,j+1}^{(g)} - \boldsymbol{p}_{i,j}^{(g)}. \tag{27}$$

Here, $a = |\boldsymbol{p}_{i,j}^{(g)} - \boldsymbol{p}_{i,j-1}^{(g)}|$, $b = |\boldsymbol{p}_{i,j+1}^{(g)} - \boldsymbol{p}_{i,j}^{(g)}|$, and $c = |\boldsymbol{p}_{i,j+1}^{(g)} - \boldsymbol{p}_{i,j-1}^{(g)}|$.

Points with a large curvature and irregular point spacing are typically spurious points that have not been removed in the previous stabilisations. To account for irregular point spacing, the curvature index is modified as

$$I_i = \kappa_i \frac{\max(a_i, b_i)}{\min(a_i, b_i)}. \tag{28}$$

Points associated with excessively large values of I_i are removed, resulting in smoother fibre trajectories while preserving the global kinematic behaviour. The threshold value of I_i is a tuning parameter that should be chosen low enough to ensure the algorithm can successfully run and high enough to prevent too aggressive smoothing. In the present study, a value of $I_{\text{th}} = 300$ is adopted. Please note that the curvature index is dimensional and depends on the selected unit system.

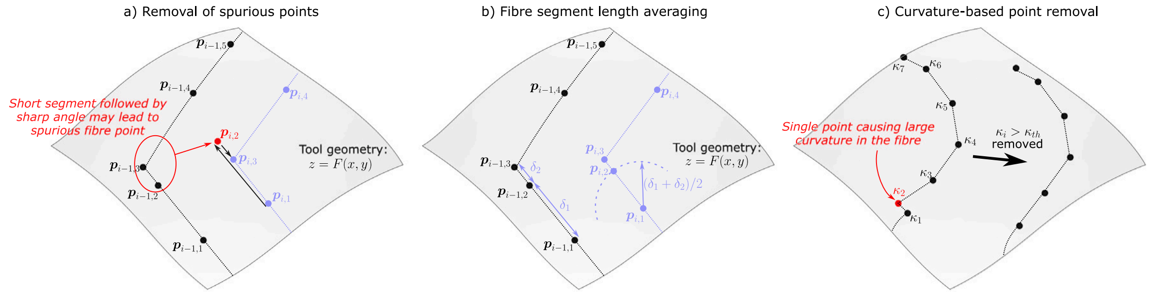

Fig. 7. Illustration of simple-shear stabilisations. (a) An obtuse angle between the vector from fibre point $\boldsymbol{p}_{i,j-1}$ to $\boldsymbol{p}_{i,j}$ and the vector from fibre point $\boldsymbol{p}_{i,j}$ to $\boldsymbol{p}_{i,j+1}$ indicate that j is a spurious fibre point that should be removed. (b) The radius of the sphere in the sphere–cylinder intersection algorithm is chosen as the average length between fibre points $\boldsymbol{p}_{i-1,j}$, $\boldsymbol{p}_{i-1,j+1}$, and $\boldsymbol{p}_{i-1,j+2}$ of the preceding fibre. (c) After all points in a fibre are placed, the points that have a local curvature exceeding a threshold value are removed.

Influence of stabilisations on the kinematic constraints. The stabilisation procedures have different roles in the fibre-tracking algorithm. The removal of spurious points prevents local reversals in the fibre path and removes non-physical points that would otherwise violate the kinematic constraints. Fibre segment length averaging regularises the step size without removing points and therefore helps preserve the discretisation before spurious points are removed. These two stabilisations should therefore always be used, as they stabilise the fibre-tracking algorithm and ensure that the kinematic constraints are satisfied. The curvature-based criterion is used to remove very short and irregular fibre segments on double-curved mould regions, which may otherwise lead to unstable fibre tracking. Since this stabilisation removes points and may locally alter the discretisation, the threshold should be chosen as high as possible while still ensuring stable fibre paths. In practice, simulations should first be attempted without curvature-based stabilisation. If instabilities occur, I_{th} should be gradually reduced until stable fibre tracking is obtained to avoid excessive smoothing of the fibre path.

2.5. Enhanced simple-shear algorithm

The enhanced simple-shear algorithm is developed to represent the forming behaviour of unidirectional fabrics. Experimental studies have shown that unidirectional non-crimp fabrics (UD-NCFs) may undergo considerable perpendicular strain during forming, in addition to in-plane shear [13]. Such deformation cannot be captured by the classical simple-shear model, which enforces a constant perpendicular fibre spacing. The enhanced simple-shear formulation replaces the constant fibre spacing constraint with a shear–spacing relation, enabling the effective spacing between neighbouring fibres to vary locally as a function of the shear deformation. This extension is directly motivated by experimental observations and enables the combined representation of shear and perpendicular deformation within a purely kinematic framework.

The algorithm builds upon the cylinder–cylinder and cylinder–sphere intersection algorithms introduced for the simple-shear model. However, the radius of the cylinders is no longer constant. Instead, it is defined locally through a shear–spacing relation that depends on the local fibre shear angle ϕ. Please note that the local fibre shear angle is computed during the fibre lay out and is distinct from the cell-based shear angle, γ, that is computed after all cells are placed as shown in Fig. 4. Even though their numeric value is identical, the sign may differ due to the way they are defined.

The local fibre shear angle ϕ is evaluated for each newly constructed point during fibre tracking. It is defined as the deviation from orthogonality between the vector

$$\boldsymbol{v}_1 = \boldsymbol{p}^{(\mathrm{g})}_{i-1,j} - \boldsymbol{p}^{(\mathrm{g})}_{i-1,j-1}, \tag{29}$$

representing the local direction of the previously constructed fibre $(i-1)$, and the vector

$$\boldsymbol{v}_2 = \boldsymbol{p}^{(\mathrm{g})}_{\mathrm{L}} - \boldsymbol{p}^{(\mathrm{g})}_{i,j-1}, \tag{30}$$

where $\boldsymbol{p}^{(\mathrm{g})}_{\mathrm{L}}$ denotes the point on fibre $(i-1)$ located at the same arc-length distance L from the fibre origin as the point $\boldsymbol{p}^{(\mathrm{g})}_{i,j-1}$ lies along fibre (i). This ensures that corresponding material points on neighbouring fibres are compared. The local fibre shear angle is then obtained as

$$\phi = 90^\circ - \angle(\boldsymbol{v}_1, \boldsymbol{v}_2), \tag{31}$$

such that $\phi = 0^\circ$ corresponds to orthogonal fibres. This geometric construction is illustrated in Fig. 8(a) and defines the local angle between the two fibres, which were initially orthogonal prior to deformation, and thus provides a measure of the local fibre shear.

For each new point in the fibre tracking algorithm, the local fibre shear angle ϕ is computed and used to update the local fibre spacing through the shear–spacing relation. Consequently, the radius of the cylinders employed in the geometric intersection is adapted pointwise, allowing the perpendicular fibre spacing to increase or decrease in response to the local shear deformation. This coupling provides a direct kinematic link between shear and perpendicular strain.

The sign of the local fibre shear angle ϕ depends on the relative location of the previous fibre. A positive shear angle is defined when the newly constructed fibre is located on the leading side of the previously constructed fibre that may be related to local fibre compression perpendicular to the fibre, whereas a negative shear angle corresponds to a trailing fibre configuration possible related with local fibre separation. This sign convention is illustrated in Fig. 8(b).

While no mechanical assumptions are embedded in this definition, the distinction between leading and trailing configurations provides a convenient framework for introducing sign-dependent variations in fibre spacing, which is later exploited to represent asymmetric spacing behaviour observed experimentally.

2.5.1. Shear-spacing relation

The enhanced simple-shear model requires a relation between the local fibre shear angle and the local transverse fibre spacing. The formulation remains purely kinematic and is introduced to reproduce experimentally observed deformation patterns rather than to represent a constitutive response. Two alternative shear–spacing relations are considered in this work, as illustrated in Fig. 8(c). The first is a physically motivated model based on the stitch geometry of the fabric, while the second is a phenomenological relation chosen to capture asymmetric spacing behaviour observed during forming.

Tricot-stitch (physical) shear-spacing relation. The physically motivated relation is derived from the geometry of the stitching used to stabilise the unidirectional fibres. For this study, fabrics stabilised by a tricot stitch are considered. The model assumes that the stitch does not

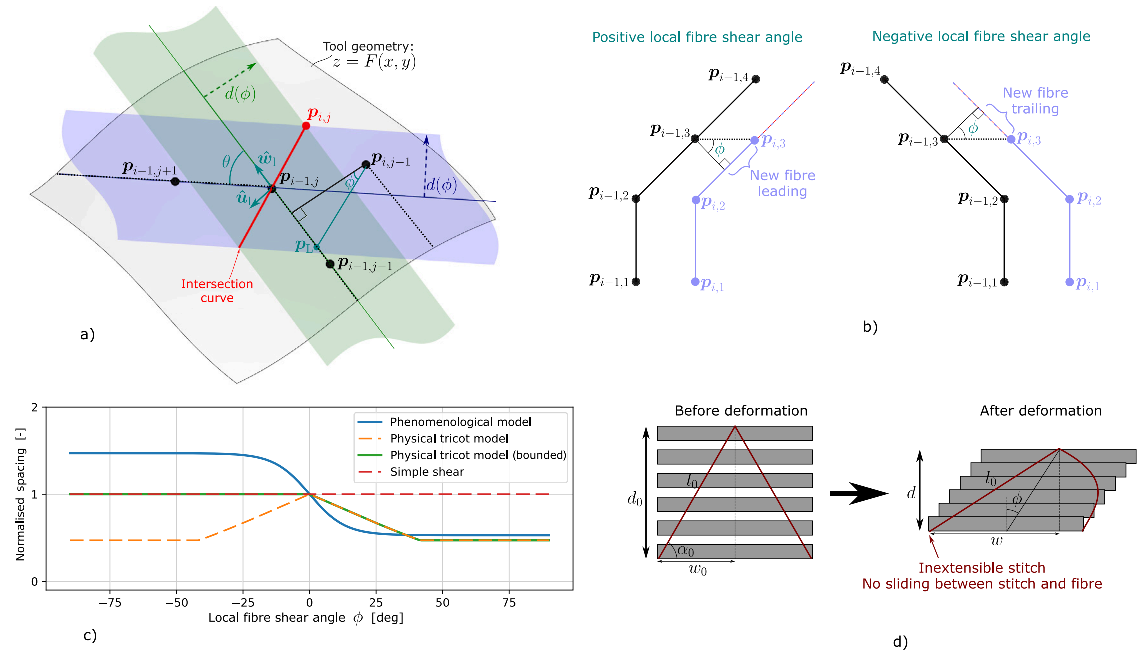

Fig. 8. Enhanced simple-shear algorithm illustrating (a) the cylinder–cylinder intersection to find new point, (b) the sign convention used to distinguish leading and trailing fibres, (c) the different shear-spacing relations considered in this paper, and (d) the tricot stitch model.

slip relative to the fibres and that the stitch is inextensible during deformation. Under these assumptions, shearing of the fibre network leads to a reduction in the effective transverse spacing between fibres as shown in Fig. 8(d). The resulting shear–spacing relation is

$$d_{\text{tri}} = d_0 \cos\phi \left(\sqrt{\cot^2 \alpha_0 \sin^2 \phi + 1} - \cot \alpha_0 \sin \phi \right), \tag{32}$$

where d_0 is the initial fibre spacing and α_0 is the tricot stitch angle. A detailed derivation of this expression is provided in Appendix C.

To prevent unphysical collapse of the fibre network at large shear angles, a minimum admissible spacing is enforced,

$$d = \max(d_{\text{tri}},\ d_{\text{lb}}), \tag{33}$$

where d_{lb} is a lower bound on fibre spacing, which is set to 0.47 for the present study. This bound can be based on physical properties of the fabric and reflects material and process constraints that limit the achievable yarn compression.

Phenomenological shear-spacing relation. While the stitch-based model captures the geometric effect of an inextensible stabilising stitch, it remains a simplified idealisation of the UD-NCF architecture. Experimental observations show that transverse spacing is also governed by stitch stretching, yarn slippage, local gapping, and yarn compaction [13]. In areas of high shear deformation, these mechanisms can lead to in-plane compaction of neighbouring fibre yarns which the physical tricot model represents. However, regions further from the main shear zone may experience tensile loading in the stitching direction. Positive perpendicular strains and visible gaps between yarns have been observed in such regions, where the stitching is under high tension. The phenomenological shear-spacing relation introduces positive spacing at negative local fibre angles which represents both compaction in high-shear zones and tension-induced gapping in regions away from the main shear zone.

To accommodate this behaviour and asymmetry in shear–spacing response within the kinematic framework, a simple phenomenological shear–spacing relation is introduced.

$$d = d_0 - \tanh(\alpha\phi) d_{\min}, \tag{34}$$

where ϕ is expressed in radians and α controls the rate at which the spacing transitions with increasing shear magnitude. α for the present study inversely calibrated as $\alpha = 4.3$. The minimum spacing is set to $d_{\min} = 0.47$, which may be determined from experiments or through parameter fitting. A sensitivity study on these parameters is presented in Section 3.2. This relation permits fibre spacing to decrease for positive local fibre shear angles and to increase for negative local fibre shear angles. The relative performance of the stitch-based and phenomenological shear–spacing relations is assessed in Section 3.2 through comparison with experimental forming results.

Damping on the shear-spacing relation. To ensure numerical stability, a simple viscous damping is applied to the transverse spacing update. This prevents abrupt changes in spacing between successive points along the fibre, which may otherwise lead to oscillations and convergence issues. The damping is introduced as a weighted update

$$d^j = \frac{\Delta t}{\eta + \Delta t} d_{\text{new}} + \frac{\eta}{\eta + \Delta t} d^{j-1}, \tag{35}$$

where d_{new} is the spacing obtained from the shear–spacing relation, d^{j-1} is the spacing from the previous step, and η is a damping coefficient taken as $\eta = 10$ in this work. In principle, Δt may be interpreted as a characteristic spatial step size, such that smaller steps lead to stronger damping. In the present implementation, however, a constant value of $\Delta t = 1$ is used for all cases.

2.6. Fabrics with rotated material orientation

For fabrics with a material orientation different from 0°, additional pre- and post-processing steps are required to recover the outer contour of the deformed fabric, as the solver discretisation is aligned with the material directions and therefore not directly applicable to arbitrarily oriented rectangular plies. To account for an initial fabric orientation of θ, a larger fabric domain, referred to here as a *superset*, is introduced in a pre-processing step, as illustrated in Fig. 9. The superset is aligned with the fibre and transverse directions and is sufficiently large to fully contain the original fabric domain for the given rotation. The kinematic solver is then applied to this superset. In a post-processing step, the results are trimmed so that only the nodes corresponding to the original fabric geometry are retained. This superset approach provides a robust and simple way to ensure that sufficient material points are available

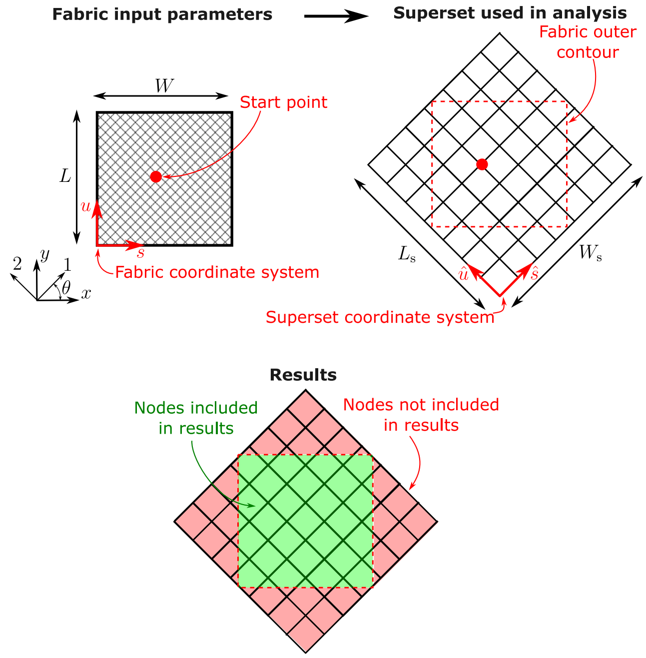

Fig. 9. Pre- and post-processing for fabric orientations different from 0°. A superset aligned with the fibre– and transverse directions is used during kinematic forming and subsequently trimmed to recover the outer contour of the deformed fabric.

for fibre tracking after rotation. A more computationally efficient implementation could instead track only the fibre segments inside the original fabric outline, but this would require additional bookkeeping to handle variable fibre lengths.

The original outer contour of the fabric can be of an arbitrary shape as long as the superset fully contains it. While the underlying method is applicable to arbitrary fabric outlines, the present implementation is limited to rectangular fabrics. The coordinate transformation from the fabric coordinate system (s, u) to the superset coordinate system $(\hat{u}, \hat{v})$ is then defined as,

$$\begin{bmatrix}\hat{s}\\ \hat{u}\end{bmatrix} = \boldsymbol{C} + \boldsymbol{R}\begin{bmatrix}s - L/2\\ u - W/2\end{bmatrix}, \tag{36}$$

where L and W are the fabric length and width, respectively, and

$$\boldsymbol{C} = \begin{bmatrix}L_S/2\\ W_S/2\end{bmatrix}, \quad \boldsymbol{R} = \begin{bmatrix}\cos\theta & -\sin\theta\\ \sin\theta & \cos\theta\end{bmatrix}. \tag{37}$$

Here, L_S and W_S denote the dimensions of the superset domain.

The origin point on the mould of the superset is modified to ensure consistency of the initial placement in cases where the draping start point in the fabric is not coinciding with a node (due to discretisation),

$$\begin{bmatrix}x_{0,S}\\ y_{0,S}\end{bmatrix} = \boldsymbol{R}\begin{bmatrix}x_0 - \Delta\hat{s}\\ y_0 - \Delta\hat{u}\end{bmatrix}, \tag{38}$$

where

$$\begin{bmatrix}\Delta\hat{s}\\ \Delta\hat{u}\end{bmatrix} = \begin{bmatrix}\hat{s} - \hat{s}_{\text{node}}\\ \hat{u} - \hat{u}_{\text{node}}\end{bmatrix}, \tag{39}$$

and $(\hat{s}, \hat{u})$ denotes the coordinates to the start point in the superset, while $(\hat{s}_{\text{node}}, \hat{u}_{\text{node}})$ denotes the coordinates to the nearest node in the superset.

2.7. Verification and validation of the kinematic models

The proposed kinematic forming framework is verified against analytical solutions and validated against both experimental measurements and high-fidelity finite element (FE) forming simulations. The objective is to assess the capability of the framework to accurately predict the forming behaviour and in-plane strains of unidirectional and biaxial non-crimp fabrics.

All validation cases consider the forming of flat fabrics over the hemispherical geometry shown in Fig. 10, corresponding to the experimental setup reported in [13].

For the kinematic analyses, a die radius of $R = 20$ mm is used instead of the $R = 5$ mm radius employed in the experiments. This choice is motivated by the representation of the mould geometry as a height function $z = F(x, y)$, which requires the surface to be single-valued in the vertical direction. For small radii, the transition region between the hemisphere and the surrounding flange approaches a near-vertical geometry, for which this representation becomes ill-defined, as multiple z-values may correspond to the same (x, y) location. Increasing the radius alleviates this issue by ensuring a well-defined surface representation across the domain, without altering the overall deformation behaviour. For the hemispherical cases considered here, the change in radius has a negligible influence on the predicted deformation and draw-in of the fabric.

Two material systems are considered: a biaxial non-crimp fabric (BIAX-NCF) and a unidirectional non-crimp fabric (UD-NCF), shown in Fig. 11 [13]. Both fabrics are manufactured from continuous carbon fibre tows and stabilised by a tricot stitch. The BIAX-NCF consists of two orthogonal fibre layers, whereas the UD-NCF comprises a single load-bearing fibre direction with stabilising glass fibres in the transverse direction for improved handleability. Despite similar areal weight of the layers, the two materials exhibit fundamentally different in-plane kinematic behaviour and therefore provide complementary test cases for assessing the proposed kinematic models.

Tam and Gutowski previously derived the analytical simple-shear solution on a hemisphere as the accumulated shear along a single fibre [48]. Here, the solutions is reformulated as a pointwise shear field on the surface as shown schematically in Fig. 10(b). This extension allows the theoretical shear values to be evaluated at any material point on the fabric, rather than only as a total value associated with an entire fibre. The associated shear angle for the field is given by,

$$\tan\gamma = \frac{x}{R}\arctan\frac{y}{z}, \tag{40}$$

where (x, y, z) denote the global coordinates on the hemisphere and R is the hemisphere radius. The derivation of this expression is provided in Appendix B and is used to verify the numerical implementation of the simple-shear algorithm.

An overview of all simulation studies considered in this work is given in Table 1. In total, five studies are conducted, each serving a distinct verification or validation purpose.

Study 1: Verification of the simple-shear model. Study 1 verifies the implementation of the simple-shear kinematic model by comparing numerical predictions with the analytical solution for forming over a hemisphere. Four simulations with increasing discretisation density are performed to assess both accuracy and convergence of the numerical solution.

A fabric size of 0.22×0.22 m is used in this study, which is sufficient to cover the hemispherical mould while limiting the extent of the flange regions. This ensures that the verification focuses on the hemisphere, as the transition to the flat region can introduce numerical sensitivities due to the abrupt change in geometry.

Study 2: Verification and calibration of the enhanced simple-shear model. Study 2a verifies the implementation of the enhanced simple-shear formulation and assesses its mesh convergence. Three checks are performed. First, the enhanced simple-shear formulation is evaluated in the special case of constant fibre spacing, $d(\phi) = d_0$, for which it should reduce to the classical simple-shear model. The resulting shear field is compared with the analytical and numerical hemispherical simple-shear solution used in Study 1. Second, the implementation of the

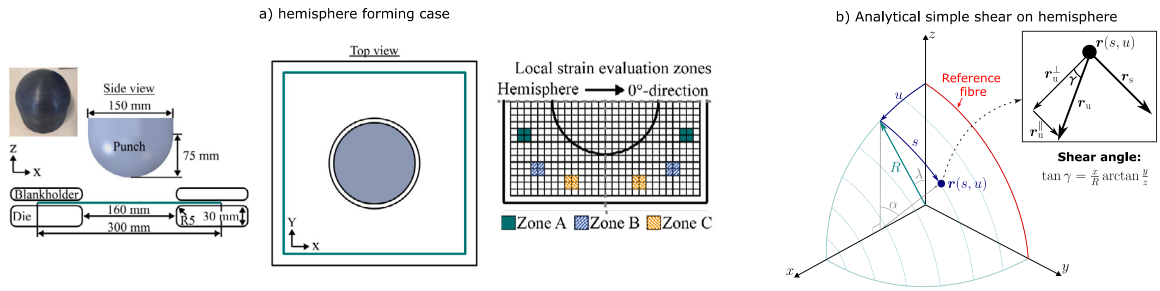

Fig. 10. (a) The hemisphere forming case used to validate the new kinematic models, reprinted from [13] licensed under CC BY 4.0. (b) Analytical simple-shear formulation used to verify the implementation of the simple-shear algorithm.

Table 1
Overview of the simulations carried out to validate the kinematic model (study 1), assess the different shear-deformation relation for the enhanced simple-shear model (study 2), and finally compare the kinematic model against experimental forming and high fidelity simulation models (studies 3–5).

Study No.	Kinematic model	No. of sims	Comparison against	Purpose
1	**Solver:** Simple-shear **Fabric orientation:** 0° **Discretisation:** 15, 31, 45, 61	4	Analytical	Verification of the simple-shear solver against analytical solution and study of the convergence of the solver.
2	**Solver:** Enhanced simple-shear **Fabric orientation:** 0° **Discretisation:** 15, 31, 45, 61, 75 **Shear-spacing relation:** Phenomenological, tricot, simple-shear	12	**Case:** $[(0°)_{UD}]$ Experimental	Verification and convergence of the enhanced simple-shear formulation, followed by calibration of the shear–spacing relation and sensitivity analysis of the phenomenological model parameters.
3	**Solver:** Pure-shear **Fabric orientation:** 0° **Discretisation:** 61	1	**Case:** $[(0°/90°)_{BIAX}]$ Experimental High fidelity Model	Reference case for BIAX-NCF forming using pure-shear kinematics.
4	**Solver:** Enhanced simple-shear **Fabric orientation:** 0° **Discretisation:** 61 **Shear-spacing relation:** Phenomenological	1	**Case:** $[(0°)_{UD}]$ Experimental High fidelity Model	Calibration-case comparison of the enhanced simple-shear model for UD-NCF 0° forming against experiments and high-fidelity FE simulations.
5	**Solver:** Enhanced simple-shear **Fabric orientation:** 45° **Discretisation:** 61 **Shear-spacing relation:** Phenomenological	1	**Case:** $[(45°)_{UD}]$ Experimental High fidelity Model	Independent validation of the calibrated enhanced simple-shear model for UD-NCF 45° forming.

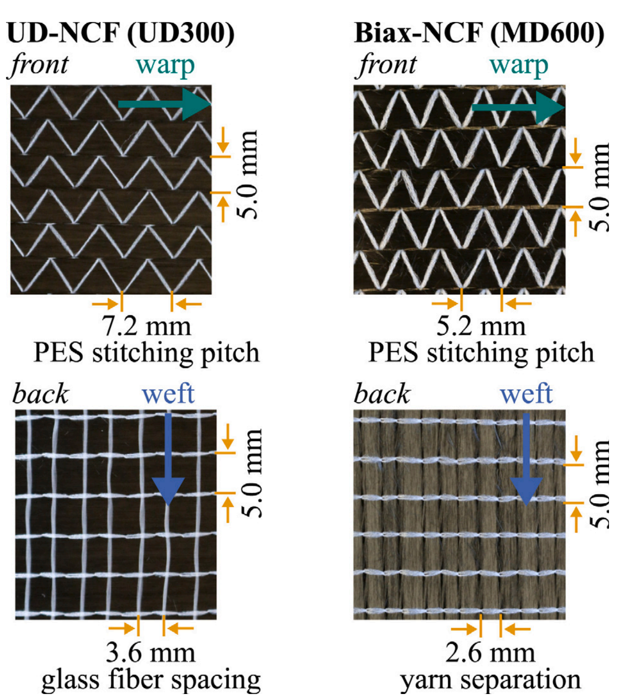

Fig. 11. Non-crimp fabrics used for the experimental forming cases presented in this paper.
Source: The figure is reprinted from [13] licensed under CC BY 4.0.

phenomenological shear–spacing relation is verified directly by prescribing local fibre shear angles and comparing the computed spacing with the analytical relation. Finally, mesh convergence of the enhanced formulation is assessed for the phenomenological shear-spacing relation using increasing discretisation densities for hemisphere forming of a UD-NCF oriented at 0°. The convergence is evaluated in terms of the contour error and the maximum shear angle.

Study 2b investigates the influence of different shear–spacing relations within the enhanced simple-shear model for a UD-NCF oriented at 0°. Multiple relations, introduced in Section 2.5, are evaluated by comparison with experimental forming results from [13]. The objective is to investigate the sensitivity of predicted geometry and strain fields to the chosen shear–spacing relation and to identify the most representable model for the material system and process considered.

Studies 3–5: Comparison with experiments and high-fidelity FE simulations. Studies 3 to 5 evaluate the predictive capability of the kinematic framework by comparison with experimental forming results and high-fidelity FE simulations reported in [13,19,49]. The FE model uses membrane elements with a hyperelastic constitutive relation specifically developed for UD-NCFs at the macro-scale and parameterised through off-axis-tensile tests [19]. Shell elements are super-imposed on the membrane elements to model a constant bending stiffness. These studies cover forming of BIAX-NCF using the pure-shear model, and UD-NCF using the enhanced simple-shear model at fabric orientations of 0° and 45°. The aim is to assess the accuracy of the kinematic approach across different reinforcement architectures and orientations, and to benchmark its performance against established FE-based forming simulations.

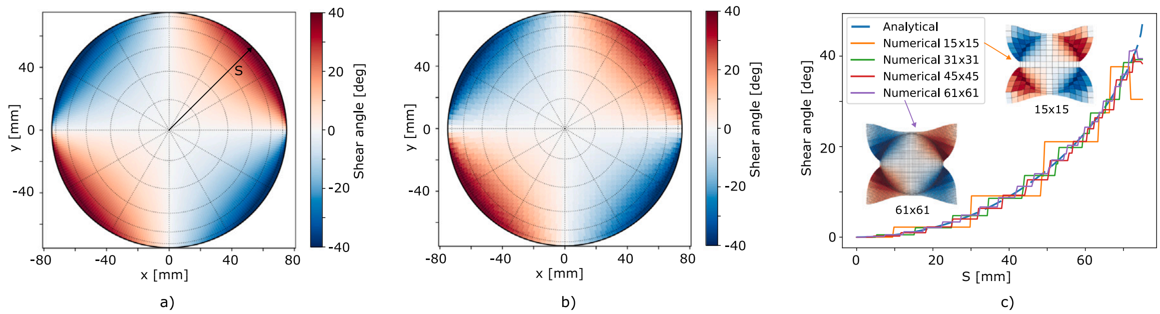

Fig. 12. Verification and convergence of the simple-shear solver for forming over a hemispherical mould: (a) analytical shear field, (b) numerical shear field for discretisation 61 × 61, and (c) comparison of shear angle along path S for increasing discretisation. Note that Study 1 uses a smaller fabric size (0.22 × 0.22 m), which is sufficient to cover the hemispherical region of interest and results in reduced flange regions compared to the other studies, thereby avoiding potential instabilities associated with excessive flange deformation.

Quantitative comparisons are performed based on the outer contours of the deformed fabric and average strain measures evaluated within the three zones indicated in Fig. 10(a).

The outer-contour error, e_c, is evaluated relative to the average experimental contour. Each of the experimental contours was resampled to $N = 400$ points uniformly distributed with respect to arc length. The starting points and indices of the contours were aligned, after which corresponding point coordinates were averaged to obtain the mean experimental contour for each experimental case, $\overline{C}_{\text{exp}}$. The model contour, C_{sim}, was resampled in the same manner. The contour error is quantified by the symmetric mean nearest-neighbour distance,

$$e_c = \frac{1}{2N}\left[\sum_{i=1}^{N}\min_j\left\|\mathbf{x}_i^{\text{sim}} - \overline{\mathbf{x}}_j^{\text{exp}}\right\|_2 + \sum_{j=1}^{N}\min_i\left\|\overline{\mathbf{x}}_j^{\text{exp}} - \mathbf{x}_i^{\text{sim}}\right\|_2\right]. \tag{41}$$

Experimental variability is quantified with the contour error between each individual experimental contour and the mean experimental contour. The reported variability error is the average of these distances over the experiments.

The strain measures are presented as an average value with standard deviation across each zone and different repetitions of the experiments. For the simulation results the strain measures are the average of several cells covering the zones. Qualitative comparisons of the strain field distributions are also presented.

All kinematic simulations are executed on a Intel® Core™ i7-10610U (4 cores, 1.80 GHz). The high-fidelity FE simulations are performed on an AMD EPYC 9374F processor (32 cores, 3.85 GHz).

3. Results

The results from the five studies outlined in Table 1 are presented in the following.

3.1. Study 1: Verification of the simple-shear solver

The verification of the simple-shear solver is shown in Fig. 12. Fig. 12(a) presents the analytical shear field for simple-shear forming of an idealised unidirectional fabric over a hemisphere, with the reference fibre aligned with the y-axis at $x = 0$. The corresponding numerical prediction obtained from the kinematic solver, using a start point at $(x_0, y_0) = (0, 0)$, an initial draping direction along the y-axis, and a discretisation of 61 × 61, is shown in Fig. 12(b).

The numerical shear field closely reproduces the analytical solution, capturing both the spatial distribution and magnitude of the shear angle. Quantitative comparison is provided in Fig. 12(c), which shows the shear angle extracted along path S for various discretisation levels. Very good agreement with the analytical solution is observed for all discretisations, thereby verifying the correct implementation of the simple-shear solver. The influence of discretisation is also evident in Fig. 12(c). While even the coarsest discretisation captures the overall shear trend accurately, local variations in shear angles are progressively resolved better as the discretisation is refined. As the kinematic solver assumes constant shear within each cell this behaviour is expected. The computational cost of running the models are 0.9 s for 15 × 15, 2.8 s for 31 × 31, 3.8 s for 45 × 45, and 4.9 s for 61 × 61. Based on this convergence study, a discretisation of 61 cells along both length and width is adopted for the remaining studies to ensure high fidelity of the predicted shear field and comparability with the high-fidelity FE results reported in [19].

3.2. Study 2: Verification and calibration of the enhanced simple-shear model

Study 2 presents both verification and convergence of the enhanced simple-shear formulation, as well as a calibration of the shear-spacing relation on the [0°] UD-NCF forming case.

3.2.1. Study 2a: Verification and convergence of the enhanced simple-shear formulation

The implementation of the enhanced simple-shear model is verified through the three numerical checks shown in Fig. 13. First, the special case of a constant fibre spacing, $d(\phi) = d_0$, is considered. In this case, the enhanced simple-shear formulation should recover the classical simple-shear solution. As shown in Fig. 13(a), the enhanced simple-shear model reproduces the analytical simple-shear solution along path S and coincides with the numerical results from the classical simple-shear formulation. This verifies that the enhanced formulation correctly reduces to the classical simple-shear when the shear-spacing relation is constant.

Second, the implementation of the shear-spacing relation is verified directly. Known local fibre shear angles ϕ are prescribed, and the resulting fibre spacing is compared with the analytical phenomenological relation. Fig. 13(b) shows that the numerical implementation reproduces the prescribed relation, thereby confirming the correct implementation of the shear-spacing relation and sign convention.

Finally, mesh convergence of the enhanced simple-shear model is assessed for the phenomenological shear-spacing relation. As shown in Fig. 13(c), the contour error decreases rapidly with increasing discretisation, from 9.1 mm for the 15 × 15 discretisation to approximately 2.2–2.4 mm for the finest discretisations. The maximum shear angle approaches a stable value, increasing from 36.2° for the 15 × 15 discretisation to 43.2° for the 75 × 75 discretisation. Based on this convergence behaviour, the 61 × 61 discretisation is considered sufficient for the subsequent simulations.

The influence of the modified transition radius was quantified by comparing simulations using $R = 20$ mm and $R = 5$ mm. The contour error changed from 2.2 mm for $R = 20$ mm to 2.5 mm for $R = 5$ mm, indicating only a minor effect on the predicted deformed outline. The

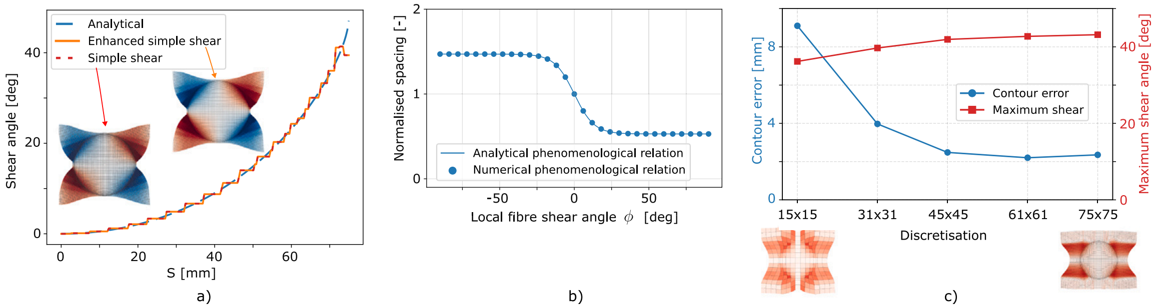

Fig. 13. Verification and convergence of the enhanced simple-shear formulation. (a) Verification of the constant-spacing case, $d(\phi) = d_0$, for which the enhanced formulation reduces to the classical simple-shear model, (b) direct verification of the implemented phenomenological shear-spacing relation, and (c) mesh convergence of the enhanced simple-shear model with the phenomenological shear-spacing relation, evaluated using the contour error and maximum shear angle for increasing discretisation densities.

larger radius is therefore used in the following analyses to improve numerical robustness, particularly for strain prediction, which may become unstable due to 'near-vertical' geometry near the transition between the hemisphere and flange.

3.2.2. Study 2b: Calibration of the shear–spacing relation

This study calibrates the shear-spacing relation for the enhanced simple shear model and examines the influence of the shear–spacing relation on the predicted forming behaviour of a UD-NCF oriented at 0°. Here and in all subsequent studies, the 0° direction is aligned with the x-axis and the starting point for the kinematic analyses are initiated from $(x_0, y_0) = (0, 0)$, while absolute shear angle values are reported to align with experimental results. Four models are evaluated: classical simple-shear, a tricot stitch-based physical shear–spacing relation, a bounded variant of the tricot relation in which simple shear is assumed for negative local fibre angles, and the proposed phenomenological relation (see Section 2.5). The computational costs are comparable for all enhanced simple-shear formulations (approximately 4.2 s), while the simple-shear solver is slightly faster (3.5 s).

The predicted outer contours of the fabric are shown in Fig. 14(a) and compared with the average experimental outer contour reported in [13]. The phenomenological model showed the closest agreement with the experiments, with a mean contour error of 2.2 mm, which is below the experimental variability of 3.5 mm. The bounded tricot model gave an error of 9.5 mm, whereas the tricot and simple-shear models produced similar and substantially larger errors of 18.2 and 18.3 mm, respectively. The simple-shear model exhibits overlap of neighbouring fibre paths in the flange regions marked with blue circles in Fig. 14(b), reflecting that simple-shear kinematics does not provide a one-to-one mapping for general mould geometries. Furthermore, the deformation of the flanges transverse to the fibre direction is significantly overpredicted due to the constant spacing constraint.

The tricot stitch-based physical shear–spacing relation accurately captures the draw-in in the fibre direction but underpredicts the transverse extension of the flanges, suggesting that the assumed fibre compaction is too large. Introducing simple-shear assumptions for negative local fibre angles improves the physical model predictions, but discrepancies with the experimental results remain near the flanges. In contrast, the phenomenological shear–spacing relation provides a close match to the experimental outer contour across the entire domain. Table 2 lists the averaged in-plane shear and perpendicular strain values in Zones A, B, and C. The locations of the zones are shown in Fig. 10. The simple-shear model strongly underpredicts shear in Zone B, overpredicts shear in Zone C, and, by construction, cannot represent perpendicular strain. The stitch-based physical shear–spacing relation overpredicts perpendicular strain in all zones and overpredicts shear in Zones B and C. Enforcing a simple-shear assumptions for negative local fibre angles improves the strain predictions in Zone C for the physical model but does not fully resolve discrepancies in the other Zones.

Table 2
Comparison of averaged in-plane shear angle and perpendicular strain in Zones A, B, and C for the UD-NCF forming experiment at 0° and the kinematic model with different shear-spacing relations. Values are reported as mean ± standard deviation over the experimental repetitions and over the corresponding evaluation zone. The experimental results are based on three repetitions.

Shear angle in degrees			
[deg]	Zone A	Zone B	Zone C
Exp	22.5 ± 4.9	21.3 ± 3.3	4.52 ± 5.9
Tricot	17.6 ± 2.0	28.4 ± 3.1	35.2 ± 16.5
Tricot b	28.4 ± 2.7	30.2 ± 7.8	14.9 ± 6.7
Pheno.	28.7 ± 2.1	24.3 ± 8.2	9.2 ± 5.7
Simple	17.6 ± 1.0	9.16 ± 3.7	12.0 ± 8.5
Perpendicular strain			
[–]	Zone A	Zone B	Zone C
Exp	−0.30 ± 0.08	−0.19 ± 0.07	−0.05 ± 0.11
Tricot	−0.54 ± 0.01	−0.52 ± 0.01	−0.17 ± 0.22
Tricot b	−0.50 ± 0.02	−0.47 ± 0.04	−0.01 ± 0.03
Pheno.	−0.39 ± 0.01	−0.35 ± 0.05	0.02 ± 0.06
Simple	0.00 ± 0.00	0.00 ± 0.00	0.00 ± 0.01

The phenomenological shear–spacing relation overpredicts perpendicular strain in Zones A and B and overpredicts shear in Zone A. Despite these local deviations, the model yields the closest overall agreement with the experimental strain data. Based on these results, the phenomenological relation is adopted for the comparison studies with UD-NCFs.

The sensitivity of the phenomenological relation to parameter variations is examined by independently increasing and decreasing each parameter by 50%. As shown in Fig. 15, the predicted outer contour is relatively insensitive to the transition-rate parameter, α: decreasing and increasing α by 50% result in mean contour errors of 3.2 and 2.3 mm, respectively. In contrast, equivalent variations in the minimum-spacing parameter, d_{min}, produce larger errors of 7.4 and 4.4 mm, respectively, which indicates greater sensitivity to this parameter.. This indicates that the overall deformation is primarily governed by the attainable range of spacing rather than the exact functional shape of the shear–spacing relation.

3.3. Studies 3–5: Comparison with experiments and high-fidelity FE simulations

This subsection presents validation of the kinematic forming framework against experimental measurements and high-fidelity finite element (FE) simulations. The comparison assesses both the predicted deformed geometry and the resulting in-plane strain fields. In the quantitative comparison, a model is considered to over- or underpredict shear and perpendicular strain if the average shear differs by more than ±5° from the experimental mean, or if the average perpendicular strain differs by more than ±0.05 from the experimental mean.

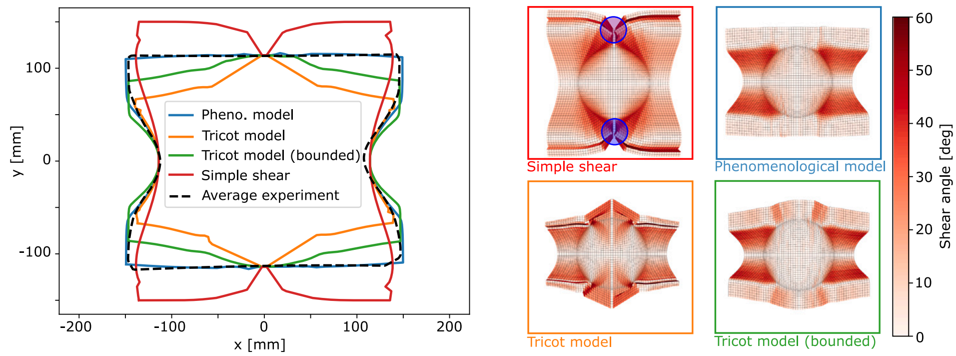

Fig. 14. (a) Predicted fabric outer contours for different shear-spacing relations using the simple-shear and enhanced simple-shear models, compared with the average experimental outer contour from three repetitions for the UD-NCF oriented at 0°. (b) Shear fields for the different shear-spacing relations. (For interpretation of the references to colour in this figure legend, the reader is referred to the web version of this article.)

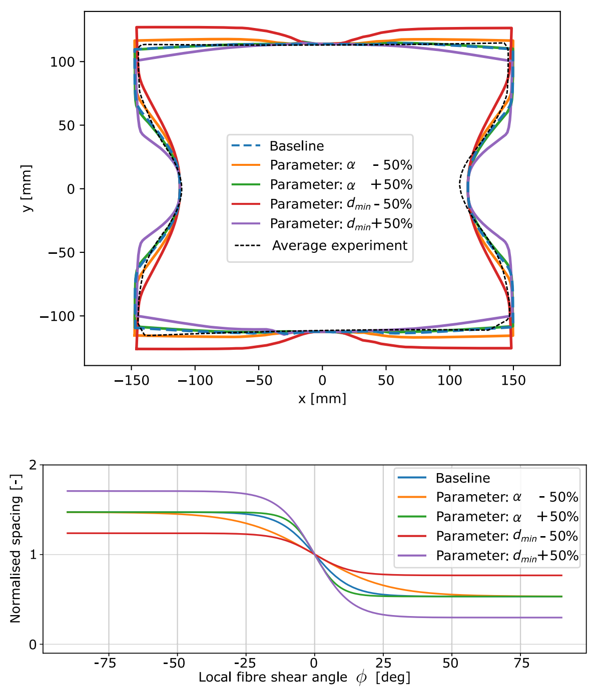

Fig. 15. Sensitivity of the predicted outer contour of the fabric to variations in the parameters of the phenomenological shear-spacing relation.

Table 3
Computational cost of the FE and kinematic models for the BIAX-NCF [0°/90°] forming case.

	1 core	16 cores	32 cores
FEM	1214 s	130 s	98 s
Kin	2.5 s	–	–

3.3.1. Reference case: BIAX-NCF [0°/90°] forming

The predicted outer contours of the fabric for forming of the BIAX-NCF [0°/90°] over a hemisphere are shown in Fig. 16, alongside the corresponding experimental results and high-fidelity FE predictions. The kinematic simulation employs the pure-shear model. The computational cost of the kinematic simulation is 2.5 s on a single CPU core, while the FE simulations require substantially higher computational effort, as summarised in Table 3.

Qualitatively, both the kinematic and FE models reproduce the experimentally observed outer contour with good agreement, as shown in Fig. 16(a). No significant deviations in draw-in or flange location are observed for either model.The kinematic simulation has a mean contour error of 4.7 mm and the FE simulation has a mean contour error of 3.5 mm. The mean experimental variability is 1.4 mm.

The corresponding in-plane shear fields are compared in Fig. 16(b) for the experiment and kinematic model, while average shear angle values evaluated in Zones A, B, and C are listed in Table 4. The pure-shear kinematic model captures the overall spatial distribution of shear observed experimentally. Quantitative comparison shows good agreement across all three zones. The FE model overpredicts shear in Zone B. Despite these local deviations, both the pure-shear kinematic model and the high-fidelity FE model reproduce the experimentally measured shear levels accurately.

Table 4
Comparison of averaged in-plane shear angles for BIAX-NCF [0°/90°] hemisphere forming. Values are reported as mean ± standard deviation over the experimental repetitions and over the corresponding evaluation zone. The experimental results are based on two repetitions.

Shear angle			
[deg]	Zone A	Zone B	Zone C
Exp	23.6 ± 7.4	32.5 ± 4.0	22.9 ± 5.8
FEM	23.5 ± 3.6	40.7 ± 5.9	23.5 ± 3.7
Kin	21.3 ± 2.7	33.1 ± 7.0	21.3 ± 2.7

Table 5
Computational cost of the FE and kinematic models for the UD-NCF [0°] forming case.

	1 core	16 cores	32 cores
FEM	1055 s	104 s	81 s
Kin	4.2 s	–	–

3.3.2. Calibration case: UD-NCF [0°] forming

The predicted outer contours for forming of the UD-NCF [0°] over the hemisphere tool are shown in Fig. 17. Results from the kinematic model employing the enhanced simple-shear assumptions with the phenomenological shear-spacing relation are compared with experimental measurements and high-fidelity FE simulations. The computational cost of the kinematic simulation is 4.2 s on a single CPU core, whereas the FE simulations require substantially higher computational effort, as summarised in Table 5.

Both numerical models reproduce the experimentally observed outer contours with good agreement. The FE model exhibits a slightly larger draw-in of the flanges compared to the kinematic model, leading to a marginally more compact final outer contour.The kinematic simulation has a mean contour error of 2.2 mm and the FE simulation has

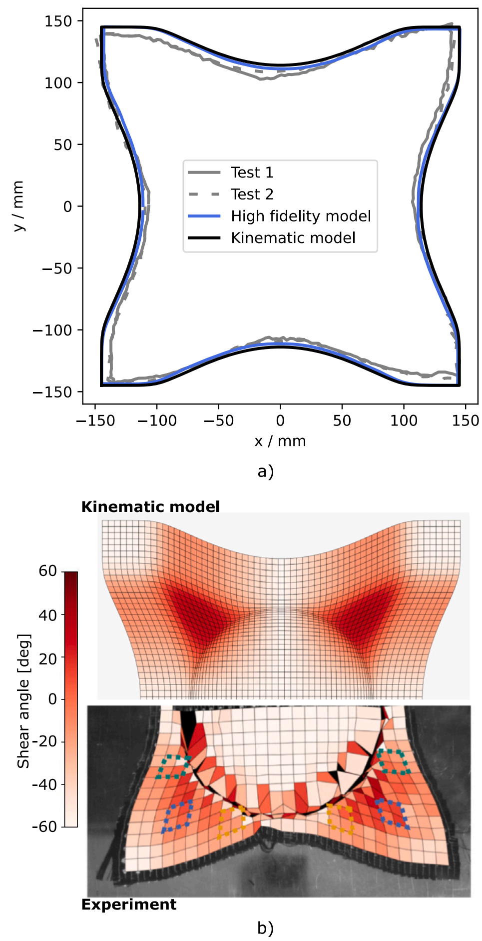

Fig. 16. (a) Comparison of deformed outer contours for BIAX-NCF [0°/90°] hemisphere forming: experiment [13], high-fidelity FE model [19], and kinematic pure-shear model. (b) Comparison of in-plane shear field for the experiment and kinematic model.

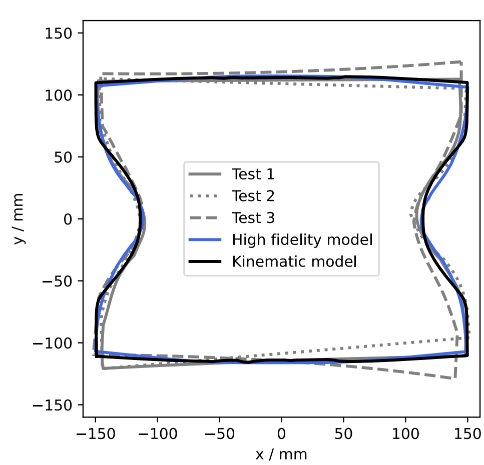

Fig. 17. Comparison of deformed outer contours for UD-NCF [0°] hemisphere forming: experiment, high-fidelity FE model, and kinematic enhanced simple-shear model.

a mean contour error of 2.9 mm. The mean experimental variability is 3.5 mm, with individual values between 2.0 and 4.8 mm.

The corresponding shear and perpendicular strain fields are shown in Fig. 18, and average values evaluated in Zones A, B, and C are listed in Table 6. Qualitatively, both models capture the main deformation patterns observed experimentally. However, differences in the distribution of strain are apparent. In the FE model, shear angle is more localised, while the kinematic model predicts shear bands extending from the hemisphere region towards the draw-in. Similarly, perpendicular strain in the FE simulation is distributed over a broader area, whereas in the kinematic model it is coincident with regions of high shear due to the imposed shear–spacing coupling, making the in-plane shear and perpendicular strains depend on each other. Quantitatively, both models provide reasonably accurate strain predictions across the three zones compared to the experimental results. The FE model underpredicts in-plane shear in zone B, overpredicts perpendicular strain in Zone B, and overpredicts both shear and perpendicular strain in Zone C. The kinematic model overpredicts perpendicular strain in Zones A and B and overpredicts shear in Zone A. Despite these local deviations, the enhanced simple-shear model captures both the magnitude and overall distribution of in-plane deformation with accuracy comparable to the high-fidelity FE simulation.

Table 6
Comparison of averaged in-plane strain measures for UD-NCF [0°] hemisphere forming. Values are reported as mean ± standard deviation over the experimental repetitions and over the corresponding evaluation zone. The experimental results are based on three repetitions.

Shear angle			
[deg]	Zone A	Zone B	Zone C
Exp	22.5 ± 4.9	21.3 ± 3.3	4.52 ± 5.9
FEM	22.7 ± 2.9	8.69 ± 3.1	10.3 ± 9.2
Kin	28.7 ± 2.1	24.3 ± 8.2	9.2 ± 5.7
Perpendicular strain			
[–]	Zone A	Zone B	Zone C
Exp	−0.30 ± 0.08	−0.19 ± 0.07	−0.05 ± 0.11
FEM	−0.30 ± 0.02	−0.25 ± 0.02	−0.26 ± 0.06
Kin	−0.39 ± 0.01	−0.35 ± 0.05	0.02 ± 0.06

Table 7
Computational cost of the FE and kinematic models for the UD-NCF [45°] forming case.

	1 core	16 cores	32 cores
FEM	1045 s	104 s	80 s
Kin	7.8 s	–	–

3.3.3. *Validation case: UD-NCF [45°] forming*

The UD-NCF [45°] case provides a transferability assessment because the calibrated shear-spacing relation is applied to a fabric orientation different from the calibration case, changing the orientation of the fibre paths relative to the mould, fabric boundary, and evaluation zones.

The predicted outer contours for forming of the UD-NCF oriented at 45° over the hemispherical tool are shown in Fig. 19. Results obtained using the kinematic model with enhanced simple-shear assumptions and the phenomenological shear-spacing relation are compared with experimental measurements and high-fidelity FE simulations. The computational cost of the kinematic simulation is 7.8 s on a single CPU core, while the FE simulations require substantially higher computational effort, as summarised in Table 7.

A high degree of agreement between the numerical predictions and the experimental outer contour is observed. Compared to the kinematic model, the FE simulation exhibits slightly greater local variation along the outer contour. These differences are minor and do not affect the overall agreement of the predicted final shape. The kinematic simulation has a mean contour error of 3.8 mm and the FE simulation has a mean contour error of 5.7 mm. The mean experimental variability is 4.0 mm, with individual values between 2.6 and 5.6 mm.

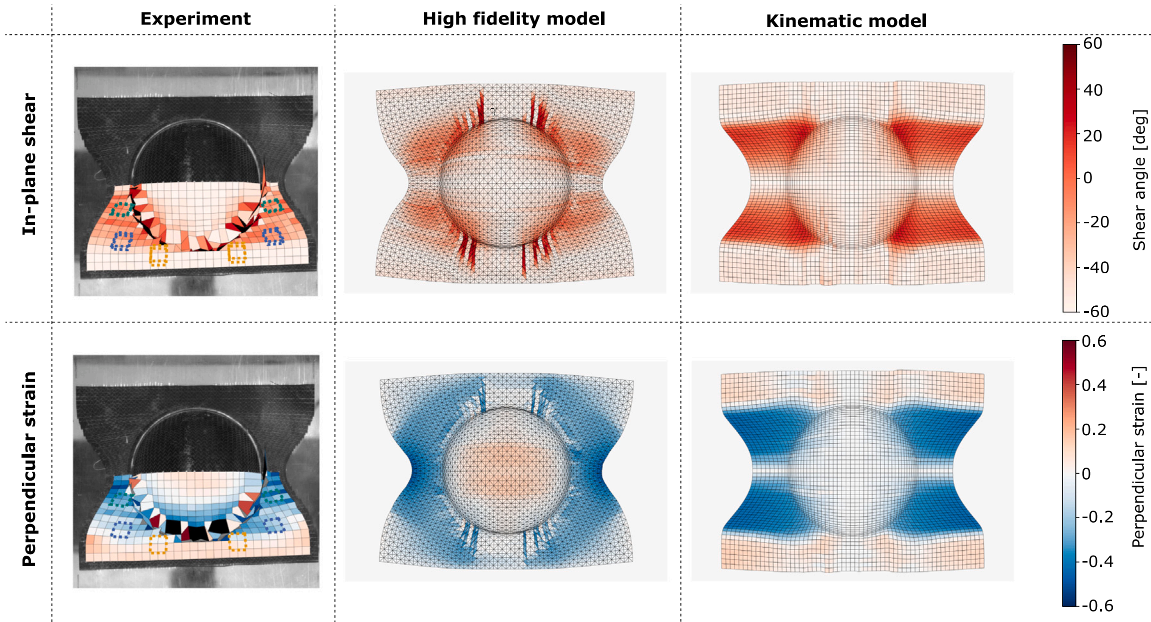

Fig. 18. Comparison of in-plane shear angle and perpendicular strain for UD-NCF [0°] hemisphere forming: experiment, high-fidelity FE model, and kinematic enhanced simple-shear model.
Source: The experimental results are reprinted from [13] licensed under CC BY 4.0.

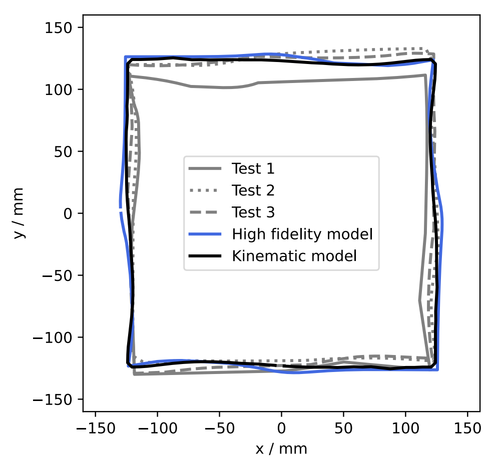

Fig. 19. Comparison of deformed outer contours for UD-NCF [45°] hemisphere forming: experiment, high-fidelity FE model, and kinematic enhanced simple-shear model.

Table 8
Comparison of averaged in-plane strain measures for UD-NCF [45°] hemisphere forming. Values are reported as mean ± standard deviation over the experimental repetitions and over the corresponding evaluation zone. The experimental results are based on three repetitions.

Shear angle			
[deg]	Zone A	Zone B	Zone C
Exp	32.6 ± 7.0	1.96 ± 1.1	27.9 ± 5.4
FEM	24.8 ± 1.9	4.56 ± 2.4	24.6 ± 2.2
Kin	28.4 ± 2.1	2.56 ± 2.3	28.4 ± 1.9
Perpendicular strain			
[–]	Zone A	Zone B	Zone C
Exp	−0.39 ± 0.07	−0.17 ± 0.05	−0.38 ± 0.10
FEM	−0.29 ± 0.02	−0.31 ± 0.02	−0.29 ± 0.02
Kin	−0.39 ± 0.01	−0.08 ± 0.07	−0.39 ± 0.01

The corresponding in-plane shear and perpendicular strain fields are shown in Fig. 20, and average strain values evaluated in Zones A, B, and C are listed in Table 8. Both numerical models predict similar in-plane shear distributions in good agreement with the experimental measurements. Differences are more pronounced in the perpendicular strain fields. In the kinematic model, perpendicular strain is locally coupled to the shear field through the shear-spacing relation and is therefore confined to regions of high shear. In contrast, the FE model predicts perpendicular strain distributed over a broader area.

Quantitative comparison in Table 8 shows that the kinematic model provides accurate predictions of shear in all zones and perpendicular strain in Zones A and C. The only discrepancy observed is for the perpendicular strain in Zone B, where the kinematic model underpredicts the experimental value. Despite this local underprediction in Zone B, the UD-NCF [45°] case provides useful transferability evidence, as the calibrated shear-spacing relation captures the overall deformation pattern and strain levels without further parameter adjustment. The FE model underpredicts shear in zone A and perpendicular strain in Zones A and C, while overpredicting perpendicular strain in Zone B.

4. Discussion

The forming simulations presented in the previous section demonstrate the capabilities and limitations of the proposed kinematic forming framework when applied to non-crimp fabrics formed over a hemispherical tool. The framework includes a robust implementation of simple-shear kinematics, verified against an analytical solution, and an enhanced simple-shear formulation that accounts for transverse deformation through a shear–spacing relation.

In the simple-shear formulation, the fabric is modelled as a set of inextensible, parallel unidirectional fibres that are free to slide relative to one another while maintaining a constant perpendicular spacing. This type of kinematic behaviour has previously been associated with unidirectional reinforcements [32,35,36]. However, experimental results for UD-NCFs show that transverse and perpendicular deformation can play a significant role during forming [13]. As demonstrated in the present study, classical simple-shear kinematics cannot represent this deformation mode, leading to inaccurate predictions of both fabric outer contour and in-plane strain fields.

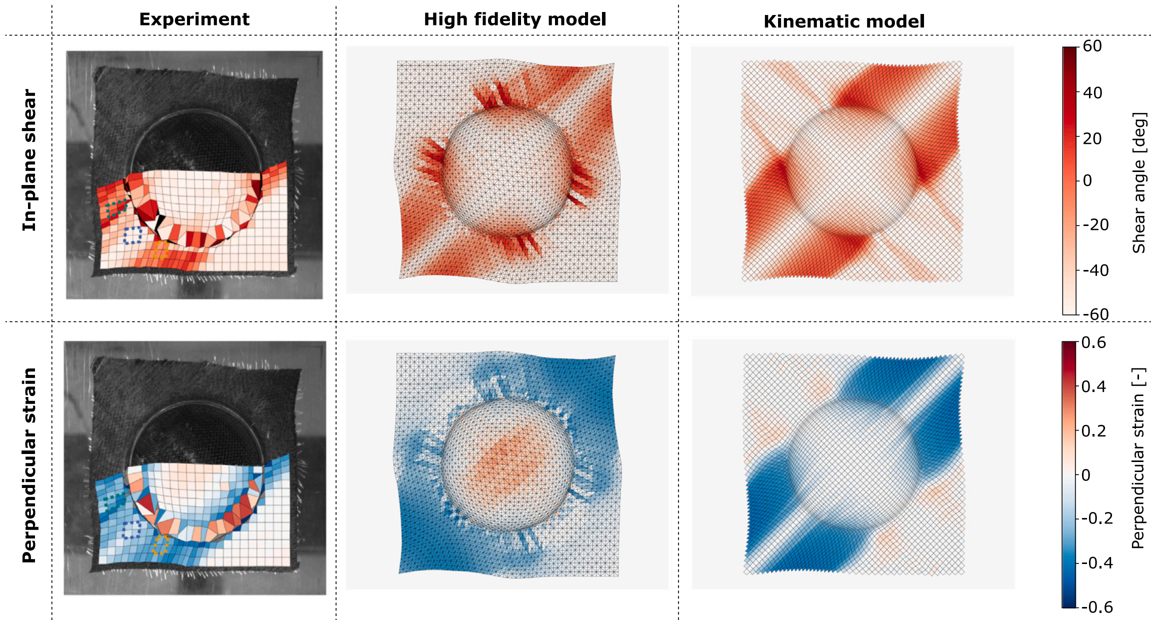

Fig. 20. Comparison of in-plane shear angle and perpendicular strain for UD-NCF [45°] hemisphere forming: experiment, high-fidelity FE model, and kinematic enhanced simple-shear model.
Source: The experimental results are reprinted from [13] licensed under CC BY 4.0.

The enhanced simple-shear formulation addresses this limitation by introducing a shear–spacing relation that links local fibre-level shear angles to transverse fibre spacing. The results show that the choice of this relation has a decisive influence on the predicted forming behaviour. A stitch-based physical relation derived from the tricot stitch geometry captures the geometric effect of an inextensible stabilising stitch, but systematically overpredicts perpendicular strain and overestimates flange draw-in. A bounded variant of this relation with classic simple-shear assumptions at negative local fibre angles improves predictions in some regions but does not fully resolve discrepancies with both strains and flange draw-in. The weak agreement of the tricot model can be attributed to its idealised assumptions: the stitch is assumed inextensible and fixed to the yarns, whereas the actual UD-NCF deformation involves stitch extensibility, yarn sliding, yarn compaction, frictional interactions, and local gapping [13,15]. These mechanisms are not represented explicitly in the tricot model and motivate the use of a phenomenological shear-spacing relation.

In contrast, the proposed phenomenological shear–spacing relation provides a consistently good description across all validation cases considered. While this relation is phenomenological rather than geometrically derived, it captures the overall deformation pattern observed experimentally, including the deformed contour and main regions of shear and perpendicular strain. The local strain magnitudes are also generally well predicted, although larger zone-wise discrepancies remain in selected regions. A plausible explanation for this is that transverse fibre spacing during forming is governed not only by the stitch configuration, but also by further material- and process-related effects. The stitch-based tricot model represents a material idealisation and does not account for stitch stretching, yarn slipping, and yarn gapping that occur during forming [13]. The phenomenological shear–spacing relation implicitly captures these combined material–process interactions without attributing them to a single physical mechanism. In the kinematic framework, negative local fibre shear corresponds to trailing fibre configurations. This geometric configuration is not itself a direct measurement of fibre separation, but it is consistent with experimentally observed fibre separation and gap formation in the flange regions during UD-NCF forming [13], which can explain why the increasing spacing for negative local fibre angles provides accurate results. As a result, the relation should be interpreted as a kinematic constraint that embeds both material behaviour and process conditions, rather than a purely material property. This also implies that the shear–spacing relation may not be universally applicable. Different forming setups, such as processes without blank holders or automated tape-laying strategies, as well as alternative stitch architectures in UD fabrics, may exhibit different transverse deformation behaviour and therefore may require alternative or re-parameterised spacing relations. Future studies will show if the relation is dependent on process and material system. In the present formulation, process effects such as out-of-plane compaction from the blank holder are not represented explicitly, but are only included indirectly through the calibrated shear–spacing relation. A possible future extension would be to make the spacing depend on both the local fibre shear angle and a compaction measure, e.g. local normal pressure, thickness change, or position relative to the blank holder.

An important observation is that the predicted forming response is insensitive to the rate at which the spacing changes with increasing shear, but sensitive to the admissible range of transverse spacing as shown in Fig. 15. The transition-rate parameter controls how rapidly the relation moves between compaction and separation, whereas the spacing-range parameter controls the maximum allowable yarn compaction and separation. For the present forming case, which involves relatively large shear angles, the spacing range has the clearer physical influence and is therefore the more important parameter to determine experimentally. For less aggressive forming cases with smaller shear angles, the transition rate may become more important because the response may remain closer to the transition region of the relation. Thus, for the hemisphere forming considered here, the enhanced simple-shear model with the phenomenological relation remains simple yet accurate, with the response effectively governed by a single dominant parameter.

The comparison with high-fidelity FE simulations clarifies the scope and limitations of the kinematic framework. The FE model represents material behaviour and process conditions explicitly and allows perpendicular deformation to occur independently of in-plane shear. As a result, perpendicular strain may appear in regions with low shear, as observed in the UD-NCF [45°] case. In contrast, the kinematic model enforces a coupling between shear and transverse deformation through the shear–spacing relation, such that perpendicular strain is directly correlated with regions of high shear. For the experimental cases investigated here, this coupling is consistent with the measured deformation patterns and leads to accurate predictions. The larger local discrepancies observed in some evaluation zones can be attributed to the kinematic model only representing transverse deformation through the local shear-spacing relation. For example, the underprediction of perpendicular strain in Zone B for the UD-NCF [45°] case suggests that this region is influenced by additional deformation mechanisms not fully captured by the calibrated relation, such as yarn compaction without yarn/fibre sliding, non-local effects, or process-history effects. Another important distinction between the kinematic and FE models lies in the representation of shear behaviour. The kinematic model introduces a direction-dependent response, where deformation along the fibres is governed by sliding, while transverse deformation is controlled by the shear–spacing relation. This results in an asymmetric shear response consistent with fibre sliding-dominated deformation mechanisms in UD-NCFs. In contrast, classical continuum formulations assume symmetric shear stiffness (e.g. $C_{1212} = C_{2121}$), which does not distinguish between these modes. This difference helps explain some of the discrepancies between the numerical models and the experimental observations in Figs. 18 and 20. Extending continuum FE models to incorporate such mechanisms, for example through roving slippage formulations, represents a promising direction to bridge this gap [50,51], although their application to forming processes remains an active area of research.

Another key distinction between the two modelling approaches is that FE simulations explicitly represent the forming process from the initial flat state to the final tool contact configuration, including transient effects, wrinkle formation, and path-dependent effects during forming. The kinematic model, by contrast, maps the fabric directly onto the final mould geometry. Like conventional pure-shear approaches, the predicted deformation depends on the choice of origin point and generators. In this study the origin point is chosen as the first contact point with the tool, which is a typical choice for the hemispherical geometry. The sensitivity to origin point and generator paths should be investigated in future studies for more complex mould geometries. While this means that process history is not directly modelled, intermediate forming states can be approximated by evaluating the mapping on a sequence of progressively developed mould geometries if required.

The principal advantage of the kinematic framework lies in its computational efficiency. For the cases studied, speed-up factors of approximately 134–251 are observed relative to the FE simulations for UD-NCF forming cases. These numbers should be interpreted in light of differences in numerical formulation and hardware utilisation. The FE simulations employ superimposed shell and membrane elements in parallel execution on multi-core architectures, while the kinematic solver is currently executed serially. Although parallelisation of the kinematic solver is possible, for example by solving the four independent quadrants in Step 3 (see Fig. 1) parallel, the primary benefit of the framework lies in reducing the computational burden at the modelling level rather than through aggressive parallelisation. An additional advantage of the proposed kinematic framework is the limited material characterisation effort required compared with more advanced constitutive forming models. The model relies primarily on geometric and kinematic assumptions and therefore avoids calibration procedures involving a large number of material parameters.

Considering the balance between accuracy and efficiency, the proposed kinematic framework is particularly well suited for applications that require a large number of forming simulations. These include draping configuration optimisation, sensitivity analyses, and iterative design workflows where qualitative trends and relative comparisons are more important than high-fidelity stress resolution. While wrinkles and out-of-plane defects cannot be resolved explicitly, shear and transverse deformation fields can serve as effective indicators for defect-prone regions. The framework may therefore be used to guide optimisation of mould geometry, draping direction, and initial placement, potentially in combination with higher-fidelity FE simulations for final validation. In addition, alternative shear-spacing relations may be evaluated to screen the influence of different material behaviour, which, together with additional experimental characterisation or high-fidelity modelling, could support future optimisation of fabric architecture. Another use case of the new framework is to use the predicted fibre orientations and strain states directly as input to subsequent structural analyses, enabling integration into virtual process chains. The improved representation of fibre kinematics and transverse spacing may also support more accurate permeability predictions in integrated virtual manufacturing chains for liquid composite moulding processes [52].

4.1. Guide for choosing the kinematic model

Based on the results presented in this study, guidance can be given on the selection of kinematic models for different reinforcement architectures. For woven fabrics, biaxial NCFs, and quasi-unidirectional NCFs at low shear angles [36], the pure-shear model is recommended. This formulation is numerically robust, requires no additional material and process relations, and provides accurate predictions for these material systems.

For unidirectional reinforcements, such as UD-NCFs and UD tapes, the enhanced simple-shear formulation is required to capture the combined effects of shear and transverse deformation. The classical simple-shear model may be interpreted as a special case of the enhanced formulation with constant fibre spacing and is generally insufficient for UD fabrics undergoing significant transverse deformation. While the phenomenological kinematic description is expected to be directly applicable to other UD systems, the shear–spacing relation may require adaptation to reflect differences in material architecture and process conditions.

Further investigation is required to assess the generality of the proposed shear–spacing relation across different materials and manufacturing processes. Forming scenarios without blank holders, as well as alternative processes such as automated tape laying, may require different kinematic shear-spacing relations. Nevertheless, the present results demonstrate that incorporating shear-dependent spacing into kinematic forming models is essential for accurately representing the forming behaviour of modern unidirectional non-crimp fabrics.

5. Conclusion

This paper has presented a new kinematic forming framework for fast and accurate prediction of the forming behaviour of unidirectional fabrics. The framework combines geodesic path generation with robust geometric solvers to enforce prescribed simple-shear kinematic assumptions on the fabric. Furthermore, it introduces an enhanced simple-shear formulation that allows transverse deformation through an experimentally calibrated shear–spacing relation.

The proposed approach was verified against analytical solutions and validated against experimental forming results and high-fidelity finite element simulations through five dedicated studies. Based on these investigations, the following conclusions can be drawn:

- The simple-shear model was successfully verified against the analytical solution for simple-shear forming over a hemispherical surface.
- Convergence studies demonstrated that even coarse discretisations capture the global shear response accurately, while finer discretisations are required to resolve local shear variations due to the assumption of constant shear within each cell.
- Classical simple-shear kinematics were shown to be insufficient for predicting the forming behaviour of UD-NCFs, as they cannot represent transverse deformation observed experimentally.

- Among the evaluated shear–spacing relations to account for transverse deformation, the proposed phenomenological relation provided the most accurate predictions of both deformed outer contour and in-plane strain fields for UD-NCF forming at 0° and 45° orientations.
- The kinematic framework achieved speed-up factors of approximately 134–251 compared with high-fidelity finite element simulations while maintaining comparable accuracy for the cases considered.

The presented framework provides a computationally lightweight alternative to finite element forming simulations, particularly well suited for early-stage design, process optimisation, and parametric studies where a large number of forming evaluations are required. While the phenomenological shear–spacing relation effectively captures the combined influence of material behaviour and process conditions for the investigated cases, further work is needed to assess its generality for other unidirectional reinforcements and manufacturing scenarios.

The kinematic forming framework developed in this paper is made freely available as open-source software at https://doi.org/10.5281/zenodo.22044780. By enabling efficient forming predictions for unidirectional fabrics, the framework contributes towards fast and scalable virtual process chains for advanced composite manufacturing.

CRediT authorship contribution statement

Peter Hede Broberg: Writing – original draft, Visualization, Validation, Software, Methodology, Formal analysis, Conceptualization. **Christian Krogh:** Writing – review & editing, Software, Methodology. **Bastian Schäfer:** Writing – review & editing, Methodology, Formal analysis. **Jan Paul Wank:** Writing – review & editing, Methodology, Formal analysis. **Luise Kärger:** Writing – review & editing, Supervision, Methodology. **Brian Lau Verndal Bak:** Writing – review & editing, Supervision, Methodology, Conceptualization. **Esben Lindgaard:** Writing – review & editing, Supervision, Methodology, Conceptualization.

Declaration of competing interest

The authors declare the following financial interests/personal relationships which may be considered as potential competing interests: Given her role as Associate Editor for Composites Part B, Luise Kärger had no involvement in the peer review of this article and had no access to information regarding its peer review. Full responsibility for the editorial process for this article was delegated to another journal editor. If there are other authors, they declare that they have no known competing financial interests or personal relationships that could have appeared to influence the work reported in this paper.

Acknowledgements

This study was completed as part of the MADE4WIND research project funded by the European Commission with project ID 101136096 from the HORIZON Europe programme. Comparison with finite element forming simulation was performed as part of the Heisenberg project no. 455807141, funded by the German Research Foundation (DFG). The authors gratefully acknowledge the support.

Appendix A. Derivation of curve intersections

A.1. Cylinder–cylinder intersection

We consider the intersection between two cylinders of equal radius r, where the second cylinder is rotated by an angle θ about the y-axis as shown in Fig. 5.

The equation of cylinder 1 is

$$x^2 + y^2 = r^2. \tag{A.1}$$

The equation of cylinder 2 is

$$(x\cos(\theta) - z\sin(\theta))^2 + y^2 = r^2. \tag{A.2}$$

Equating the two equations:

$$(x\cos(\theta) - z\sin(\theta))^2 = x^2. \tag{A.3}$$

Taking the square root:

$$x\cos(\theta) - z\sin(\theta) = \pm x. \tag{A.4}$$

Solving for z:

$$z = x\left(\frac{\cos(\theta) \pm 1}{\sin(\theta)}\right). \tag{A.5}$$

Further simplifying:

$$z = x\left(\frac{\cos(\theta)}{\sin(\theta)} \pm \frac{1}{\sin(\theta)}\right) = x\left(\cot(\theta) \pm \csc(\theta)\right). \tag{A.6}$$

The intersection curve can therefore be parameterised as:

$$x = r\cos(t) \tag{A.7}$$

$$y = r\sin(t) \tag{A.8}$$

$$z = x\left(\cot(\theta) \pm \csc(\theta)\right). \tag{A.9}$$

A.2. Cylinder-sphere intersection

We consider the intersection between a cylinder of radius r and a sphere of radius R, whose centre is offset by a along the x-axis as shown in Fig. 6.

The equation of the cylinder is

$$x^2 + y^2 = r^2. \tag{A.10}$$

The equation of the sphere is

$$(x-a)^2 + y^2 + z^2 = R^2. \tag{A.11}$$

Combining the two equations:

$$x^2 + y^2 - (x-a)^2 - y^2 - z^2 = r^2 - R^2, \tag{A.12}$$

which simplifies to

$$2ax = z^2 + a^2 + r^2 - R^2. \tag{A.13}$$

Rewriting:

$$z^2 = 2a(x-b), \tag{A.14}$$

where

$$b = \frac{a^2 + r^2 - R^2}{2a} \tag{A.15}$$

is the x-coordinate of the vertex of the resulting parabola in the (x, z)-plane. Solving for z:

$$z = \pm\sqrt{2a(x-b)} \tag{A.16}$$

The intersection curve is thus parameterised as:

$$x = r\cos(t) \tag{A.17}$$

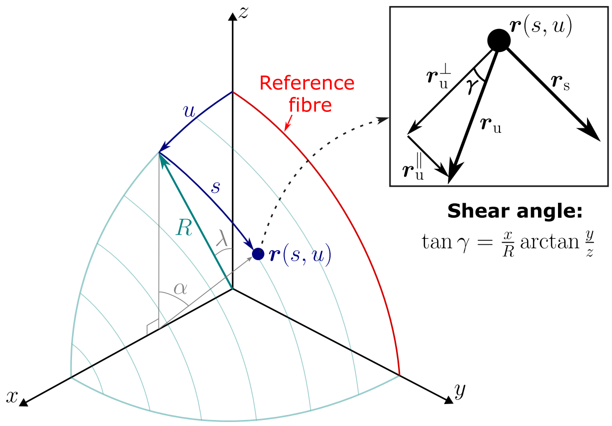

Fig. B.21. Parametrisation of the hemisphere and associated coordinate directions used for the analytical simple-shear solution.

$$y = r\sin(t) \tag{A.18}$$

$$z = \pm\sqrt{2a(x-b)} \tag{A.19}$$

with the admissible range given by $-t_0 < t < t_0$, where $\cos(t_0) = b/r$, ensuring that the argument of the square root remains non-negative.

Appendix B. Derivation of analytical simple-shear on hemisphere

We consider a reference fibre aligned with the meridian in the zy-plane as shown in Fig. B.21. The surface of the hemisphere is parameterised in terms of the coordinates s (along the fibre) and u (transverse to the fibre) as

$$\boldsymbol{r}(s,u) = \begin{bmatrix} R\sin\lambda \\ R\cos\lambda\sin\alpha \\ R\cos\lambda\cos\alpha \end{bmatrix}, \quad \lambda = \frac{u}{R}, \quad \alpha = \frac{s}{R\cos\lambda}. \tag{B.1}$$

The tangent along the fibre direction is given by

$$\boldsymbol{r}_{\mathrm{s}} = \frac{\partial \boldsymbol{r}}{\partial s} = \begin{bmatrix} 0 \\ \cos\alpha \\ -\sin\alpha \end{bmatrix}, \tag{B.2}$$

and the transverse direction is

$$\boldsymbol{r}_{\mathrm{u}} = \frac{\partial \boldsymbol{r}}{\partial u} = \begin{bmatrix} \cos\lambda \\ \sin\lambda(\alpha\cos\alpha - \sin\alpha) \\ -\sin\lambda(\cos\alpha + \alpha\sin\alpha) \end{bmatrix}. \tag{B.3}$$

The vector $\boldsymbol{r}_{\mathrm{u}}$ is decomposed into a component parallel to $\boldsymbol{r}_{\mathrm{s}}$ and a perpendicular component,

$$\boldsymbol{r}_{\mathrm{u}}^{\parallel} = (\boldsymbol{r}_{\mathrm{u}}\cdot\boldsymbol{r}_{\mathrm{s}})\boldsymbol{r}_{\mathrm{s}}, \quad \boldsymbol{r}_{\mathrm{u}}^{\perp} = \boldsymbol{r}_{\mathrm{u}} - (\boldsymbol{r}_{\mathrm{u}}\cdot\boldsymbol{r}_{\mathrm{s}})\boldsymbol{r}_{\mathrm{s}}. \tag{B.4}$$

The local shear angle is then defined from this decomposition as

$$\tan\gamma = \frac{\|\boldsymbol{r}_{\mathrm{u}}^{\parallel}\|}{\|\boldsymbol{r}_{\mathrm{u}}^{\perp}\|}. \tag{B.5}$$

It can be shown that

$$\|\boldsymbol{r}_{\mathrm{u}}^{\perp}\| = 1, \tag{B.6}$$

while

$$\|\boldsymbol{r}_{\mathrm{u}}^{\parallel}\| = \boldsymbol{r}_{\mathrm{u}}\cdot\boldsymbol{r}_{\mathrm{s}}. \tag{B.7}$$

Hence,

$$\tan\gamma = \boldsymbol{r}_{\mathrm{u}}\cdot\boldsymbol{r}_{\mathrm{s}} = \alpha\sin\lambda. \tag{B.8}$$

Expressing the result in Cartesian coordinates using $x = R\sin\lambda \rightarrow \sin\lambda = x/R$ and $\tan\alpha = y/z \rightarrow \alpha = \arctan y/z$ gives

$$\tan\gamma = \frac{x}{R}\arctan\frac{y}{z}. \tag{B.9}$$

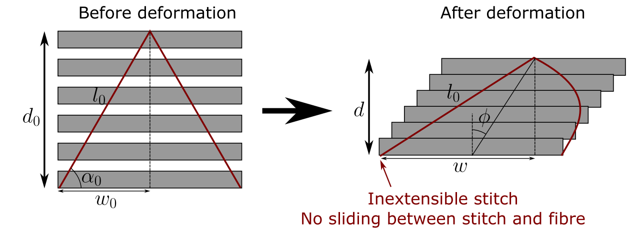

Fig. C.22. The tricot stitch model used to relate transverse spacing to shear deformation.

Appendix C. Derivation of physical tricot model

We consider a geometric representation of the tricot stitch, where the stitch length l_0 is assumed constant during deformation as shown in Fig. C.22. The initial configuration is given by

$$l_0 = \frac{d_0}{\sin\alpha_0}, \quad w_0 = d_0\cot\alpha_0, \tag{C.1}$$

where d_0 is the initial transverse spacing and α_0 is the initial stitch angle. During deformation, the projection of the stitch onto the fibre direction changes from w_0 in the initial condition to w giving

$$w = w_0 + d\tan\phi = d_0\cot\alpha_0 + d\tan\phi, \tag{C.2}$$

where ϕ is the local fibre shear angle. Using Pythagoras' theorem on the deformed configuration, assuming constant stitch length $l_0^2 = w^2 + d^2$, gives

$$\frac{d_0^2}{\sin^2\alpha_0} = (d_0\cot\alpha_0 + d\tan\phi)^2 + d^2. \tag{C.3}$$

Expanding and simplifying yields the quadratic equation

$$d^2 + 2d_0\cot\alpha_0\sin\phi\cos\phi d - d_0^2\cos^2\phi = 0. \tag{C.4}$$

Taking the physically admissible (positive) root, the transverse spacing is obtained as

$$d = d_0\cos\phi\left(\sqrt{\cot^2\alpha_0\sin^2\phi + 1} - \cot\alpha_0\sin\phi\right). \tag{C.5}$$

Data availability

Link to the software repository provided in the text

KinDrape3D (Original data) (GitHub)

References

[1] Govignon Q, Bickerton S, Kelly P. Liquid composite molding processes. Elsevier; 2022, p. 101–36. http://dx.doi.org/10.1016/B978-0-12-820346-0.00006-X.

[2] Razali N, Mansor MR, Omar G, Kamarulzaman SAFS, Zin MH, Razali N. Out-of-autoclave as a sustainable composites manufacturing process for aerospace applications. Elsevier; 2021, p. 395–413. http://dx.doi.org/10.1016/B978-0-12-819482-9.00011-3.

[3] Ekuase OA, Anjum N, Eze VO, Okoli OI. A review on the out-of-autoclave process for composite manufacturing. 2022, http://dx.doi.org/10.3390/jcs6060172.

[4] Boisse P, Hamila N, Vidal-Sallé E, Dumont F. Simulation of wrinkling during textile composite reinforcement forming, Influence of tensile, in-plane shear and bending stiffnesses. Compos Sci Technol 2011;71(5):683–92. http://dx.doi.org/10.1016/j.compscitech.2011.01.011.

[5] Lightfoot JS, Wisnom MR, Potter K. Defects in woven preforms: Formation mechanisms and the effects of laminate design and layup protocol. Compos Part A: Appl Sci Manuf 2013;51:99–107. http://dx.doi.org/10.1016/j.compositesa.2013.04.004.

[6] Boisse P, Colmars J, Hamila N, Naouar N, Steer Q. Bending and wrinkling of composite fiber preforms and prepregs. a review and new developments in the draping simulations. Compos Part B: Eng 2018;141:234–49. http://dx.doi.org/10.1016/j.compositesb.2017.12.061.

[7] Bender J, Hallett S, Lindgaard E. Parametric study of the effect of wrinkle features on the strength of a tapered wind turbine blade sub-structure. Compos Struct 2019;218:120–9. http://dx.doi.org/10.1016/j.compstruct.2019.02.065.

[8] Thompson AJ, Belnoue JP-H, Hallett SR. Modelling defect formation in textiles during the double diaphragm forming process. Compos Part B: Eng 2020;202:108357. http://dx.doi.org/10.1016/j.compositesb.2020.108357.

[9] Broberg PH, Lindgaard E, Krogh C, Thompson AJ, Belnoue JPH, Hallett SR, Bak BLV. That's how the preform crumples: Wrinkle creation during forming of thick binder-stabilised stacks of non-crimp fabrics. Compos Part B: Eng 2024;273:111269. http://dx.doi.org/10.1016/j.compositesb.2024.111269.

[10] Lomov SV, Belov EB, Bischoff T, Ghosh SB, Chi TT, Verpoest I. Carbon composites based on multiaxial multiply stitched preforms. Part 1. geometry of the preform. Compos Part A 2002;33:1171–83. http://dx.doi.org/10.1016/S1359-835X(02)00090-8.

[11] Truong TC, Vettori M, Lomov S, Verpoest I. Carbon composites based on multi-axial multi-ply stitched preforms. part 4. mechanical properties of composites and damage observation. Compos Part A: Appl Sci Manuf 2005;36:1207–21. http://dx.doi.org/10.1016/j.compositesa.2005.02.004.

[12] Chen S, McGregor OP, Harper LT, Endruweit A, Warrior NA. Defect formation during preforming of a bi-axial non-crimp fabric with a pillar stitch pattern. Compos Part A: Appl Sci Manuf 2016;91:156–67. http://dx.doi.org/10.1016/j.compositesa.2016.09.016.

[13] Schäfer B, Zheng R, Colmars J, Platzer A, Naouar N, Boisse P, Kärger L. Experimental analysis of the forming behavior of uni-and bidirectional non-crimp fabrics for different geometries. Compos Part B 2024;287:111765. http://dx.doi.org/10.1016/j.compositesb.2024.111765.

[14] Chen S, Talokder T, Mahadik Y, Thompson A, Hallett S, Belnoue J. Preform variability propagation in non-crimp fabric (ncf) forming. Compos Part B: Eng 2025;299. http://dx.doi.org/10.1016/j.compositesb.2025.112418.

[15] Ghazimoradi M, Trejo EA, Carvelli V, Butcher C, Montesano J. Deformation characteristics and formability of a tricot-stitched carbon fiber unidirectional non-crimp fabric. Compos Part A: Appl Sci Manuf 2021;145. http://dx.doi.org/10.1016/j.compositesa.2021.106366.

[16] Stojkovic M, Butt J. Industry 4.0 implementation framework for the composite manufacturing industry. J Compos Sci 2022;6. http://dx.doi.org/10.3390/jcs6090258.

[17] Yu F, Chen S, Harper LT, Warrior NA. Simulating the effect of fabric bending stiffness on the wrinkling behaviour of biaxial fabrics during preforming. Compos Part A: Appl Sci Manuf 2020;143. http://dx.doi.org/10.1016/j.compositesa.2021.106308, 2021.

[18] Chen B, Colmars J, Naouar N, Boisse P. A hypoelastic stress resultant shell approach for simulations of textile composite reinforcement forming. Compos Part A 2021;149:106558. http://dx.doi.org/10.1016/j.compositesa.2021.106558.

[19] Schäfer B, Dörr D, Zheng R, Naouar N, Kärger L. A hyperelastic approach for modeling the membrane behavior in finite element forming simulation of unidirectional non-crimp fabrics (ud-ncf). Compos Part A: Appl Sci Manuf 2024;185. http://dx.doi.org/10.1016/j.compositesa.2024.108359.

[20] Broberg PH, Lindgaard E, Thompson AJ, Belnoue JP-H, Hallett SR, Bak BLV. An accurate forming model for capturing the nonlinear material behaviour of multilayered binder-stabilised fabrics and predicting fibre wrinkling. Compos: Part B 2024;274:111268. http://dx.doi.org/10.1016/j.compositesb.2024.111268.

[21] Bussetta P, Correia N. Numerical forming of continuous fibre reinforced composite material: A review. Compos Part A: Appl Sci Manuf 2018;113(July):12–31. http://dx.doi.org/10.1016/j.compositesa.2018.07.010.

[22] Thompson AJ, Said BE, Belnoue JP, Hallett SR. Modelling process induced deformations in 0/90 non-crimp fabrics at the meso-scale. Compos Sci Technol 2018;168:104–10. http://dx.doi.org/10.1016/j.compscitech.2018.08.029.

[23] Zheng R, Naouar N, Colmars J, Platzer A, Schäfer B, Morestin F, Kärger L, Boisse P. Mesoscopic finite element modeling of biaxial non-crimp fabric including representative stitch pattern. Compos Struct 2024;339:118126. http://dx.doi.org/10.1016/j.compstruct.2024.118126.

[24] Gomez-Flores A, Cho H, Hong G, Nam H, Kim H, Chung Y. A critical review on machine learning applications in fiber composites and nanocomposites: Towards a control loop in the chain of processes in industries. Mater Des 2024;245. http://dx.doi.org/10.1016/j.matdes.2024.113247.

[25] Middelhoff J, Dröder K, Hürkamp A. Machine learning approach for the prediction of forming results of fiber-reinforced thermoplastic composites using simulation and curvature data. Mater Des 2025;257. http://dx.doi.org/10.1016/j.matdes.2025.114418.

[26] Viisainen JV, Yu F, Codolini A, Chen S, Harper LT, Sutcliffe MP. Rapidly predicting the effect of tool geometry on the wrinkling of biaxial NCFs during composites manufacturing using a deep learning surrogate model. Compos Part B: Eng 2022;253. http://dx.doi.org/10.1016/j.compositesb.2023.110536, 2023.

[27] Zimmerling C, Dörr D, Henning F, Kärger L. A machine learning assisted approach for textile formability assessment and design improvement of composite components. Compos Part A: Appl Sci Manuf 2019;124(May):105459. http://dx.doi.org/10.1016/j.compositesa.2019.05.027.

[28] Zimmerling C, Poppe C, Stein O, Kärger L. Optimisation of manufacturing process parameters for variable component geometries using reinforcement learning. Mater Des 2022;214:110423. http://dx.doi.org/10.1016/j.matdes.2022.110423.

[29] Chen S, Thompson AJ, Dodwell TJ, Hallett SR, Belnoue JP. But how can i optimise my high-dimensional problem with only very little data? – a composite manufacturing application. Int J Solids Struct 2024;300:112941. http://dx.doi.org/10.1016/j.ijsolstr.2024.112941.

[30] Würth T, Freymuth N, Mitsch J, Dahlinger P, Hoang T, Neumann G, Kärger L. Algebraic hierarchical graph neural networks for forming simulation of thermoplastic composite materials. Key Eng Mater 2026;1050:31–42. http://dx.doi.org/10.4028/p-kaH2TN.

[31] Wang J, Paton R, Page JR. The draping of woven fabric preforms and prepregs for production of polymer composite components. Compos Part A 1999;30:757–65. http://dx.doi.org/10.1016/S1359-835X(98)00187-0.

[32] Lim T-C, Ramakrishna S. Modelling of composite sheet forming: a review. Compos Part A 2002;33:515–37. http://dx.doi.org/10.1016/S1359-835X(01)00138-5.

[33] Krogh C, Bak BLV, Lindgaard E, Olesen AM, Hermansen SM, Broberg PH, Kepler JA, Lund E, Jakobsen J. A simple MATLAB draping code for fiber-reinforced composites with application to optimization of manufacturing process parameters. 2021, p. 457–71. http://dx.doi.org/10.1007/s00158-021-02925-z.

[34] Mack C, Taylor H. 39 - the fitting of woven cloth to surfaces. J Text Inst Trans 2018;47:477–88. http://dx.doi.org/10.1080/19447027.1956.10750433.

[35] Pourtier J, Duchamp B, Kowalski M, Wang P, Legrand X, Soulat D. Two-way approach for deformation analysis of non-crimp fabrics in uniaxial bias extension tests based on pure and simple shear assumption. Int J Mater Form 2019;12:995–1008. http://dx.doi.org/10.1007/s12289-019-01481-8.

[36] Krogh C, Kepler JA, Jakobsen J. Pure and simple: investigating the in-plane shear kinematics of a Quasi-unidirectional glass fiber non-crimp fabric using the bias-extension test. Int J Mater Form 2021;14(6):1483–95. http://dx.doi.org/10.1007/s12289-021-01642-8.

[37] Ghazimoradi M, Trejo EA, Butcher C, Montesano J. Characterizing the macroscopic response and local deformation mechanisms of a unidirectional non-crimp fabric. Compos Part A: Appl Sci Manuf 2022;156. http://dx.doi.org/10.1016/j.compositesa.2022.106857.

[38] Kahavita KD, McCarthy ED, Zhang M, Brádaigh CM, Harrison P. Characterising the shear, stretch and in-plane bending response of a pure-unidirectional non-crimp fabric. Int J Mater Form 2026;19. http://dx.doi.org/10.1007/s12289-026-01978-z.

[39] Weeën FVD. Algorithms for draping fabrics on doubly-curved surfaces. Internat J Numer Methods Engrg 1991;31:1415–26. http://dx.doi.org/10.1002/nme.1620310712.

[40] Aono M, Breen DE, Wozny MJ. Fitting a woven-cloth model to a curved surface: mapping algorithms. Comput Aided Des 1994;26:278–92. http://dx.doi.org/10.1016/0010-4485(94)90074-4.

[41] Ramgulam RB. A novel algorithm for fitting a woven-cloth to complex surfaces. Int J Cloth Sci Technol 2001;13:198–207. http://dx.doi.org/10.1108/09556220110396551.

[42] Potluri P, Sharma S, Ramgulam R. Comprehensive drape modelling for moulding 3D textile preforms. Compos Part A 2001;32:1415–24. http://dx.doi.org/10.1016/S1359-835X(01)00040-9.

[43] Klintworth J, Long A. The use of draping simulation in composite design. 1st ed.. Woodhead Publishing Limited; 2007, p. 714–57. http://dx.doi.org/10.1533/9781845692537.277.

[44] Fengler B, Kärger L, Henning F, Hrymak A. Multi-objective patch optimization with integrated kinematic draping simulation for continuous–discontinuous fiber-reinforced composite structures. J Compos Sci 2018;2. http://dx.doi.org/10.3390/jcs2020022.

[45] Denkena B, Schmidt C, Werner S, Schwittay D. Development of a shape replicating draping unit for continuous layup of unidirectional non-crimp fabrics on complex surface geometries. J Compos Sci 2021;5. http://dx.doi.org/10.3390/jcs5040093.

[46] ANSYS Inc. ACP theory reference. release 2025 r1 ed.. Canonsburg, PA, USA: ANSYS, Inc; 2025, proprietary software documentation. URL https://ansyshelp.ansys.com/public/Views/Secured/corp/v251/en/pdf/Composites_Theory_Reference.pdf.

[47] Conte SD, de Boor C. Elementary numerical analysis: An algorithmic approach. In: International series in pure and applied mathematics. 3rd ed.. New York: McGraw-Hill Book Company; 1980.

[48] Tam AS, Gutowski TG. The kinematics for forming ideal aligned fibre composites into complex shapes. Compos Manuf 1990;1:219–28. http://dx.doi.org/10.1016/0956-7143(90)90044-W.

[49] Schäfer B, Dörr D, Naouar N, Wank JP, Kärger L. Capabilities and limitations of pure-shear based macroscopic forming simulations for 0°/90° biaxial non-crimp fabrics. In: Materials research proceedings. vol. 54, Association of American Publishers; 2025, p. 554–63. http://dx.doi.org/10.21741/9781644903599-60.

[50] Wank JP, Schäfer B, Mitsch J, Kärger L. Strain gradient calculation as a basis for localized roving slip prediction in macroscopic forming simulation of non-crimp fabrics. In: Materials research proceedings. vol. 41, Association of American Publishers; 2024, p. 467–76. http://dx.doi.org/10.21741/9781644903131-52.

[51] Wank JP, Schäfer B, Kärger L. Accounting for roving slippage in the macroscopic forming simulation of unidirectional non-crimp fabrics. Compos Part A: Appl Sci Manuf 2026;206. http://dx.doi.org/10.1016/j.compositesa.2026.109746.

[52] Lu X, Ding J, Peng X, Sun G, Wang X, Yue W, Zhou H, Huang Z, Zhou H, Mai YW. A focused review of the draping process and its impact on the resin infusion in liquid composite molding. Thin-Walled Struct 2024;205. http://dx.doi.org/10.1016/j.tws.2024.112362.